

EXPLORING THE FLAME CHEMISTRY OF C₅ TETRAHYDROFURANIC BIOFUELS: TETRAHYDROFURFURYL ALCOHOL AND 2-METHYLTETRAHYDROFURAN

Luc-Sy Tran^{1,*}, Hans-Heinrich Carstensen^{2,3,*}, Nathalie Lamoureux¹, Kae Ken Foo¹, Sylvie Gosselin¹, Abderrahman El Bakali¹, Laurent Gasnot¹, Pascale Desgroux¹

¹ Univ. Lille, CNRS, UMR 8522 - PC2A - Physicochimie des Processus de Combustion et de l'Atmosphère, F-59000 Lille, France

² Fundación Agencia Aragonesa para la Investigación y Desarrollo (ARAID), Zaragoza, Spain

³ Department of Chemical and Environmental Engineering, Engineering and Architecture School, University of Zaragoza, Spain

* Corresponding author:

Dr. Luc-Sy Tran
Univ. Lille, CNRS, UMR 8522 - PC2A - Physicochimie des Processus de Combustion et de l'Atmosphère, F-59000 Lille, France.
E-mail: luc-sy.tran@univ-lille.fr

Dr. Hans-Heinrich Carstensen,
University of Zaragoza, Department of Chemical and Environmental Engineering
C/ Maria de Luna 2
50018 Zaragoza, Spain
E-mail: hcarsten@posta.unizar.es

Full-Length Article

Color figures in electronic version only

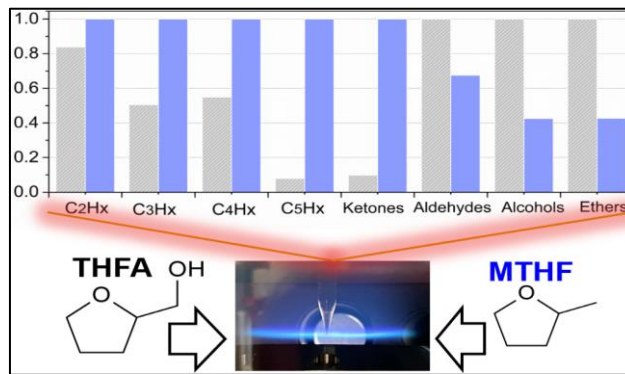
Three Supplemental Information Available:

1/ Supplemental information (PDF)

2/ Kinetic model (Text)

3/ Experimental data (Excel)

TOC Graphic



Abstract

Recently, the combustion chemistry of tetrahydrofurfuryl alcohol (THFA), a potential biofuel, was investigated in a stoichiometric 20 mole-% THFA/methane co-fueled premixed flame at 5.3 kPa by our group [Tran *et al.* Proc. Combust. Inst. 38 (2021) 631–640]. With regard to this, we continue to explore further the combustion chemistry of this biofuel in order to understand the influence of THFA doping amounts on the flame chemistry of its mixture with methane, and the impact of the alcohol function of THFA on the product spectrum compared to its non-alcoholic fuel counterpart, *i.e.* 2-methyltetrahydrofuran (MTHF). To accomplish the above said objective, a methane flame, a 10% THFA/methane flame, and a 20% MTHF/methane flame were additionally analyzed at similar conditions using gas chromatography for quantitative species detection and NO-LIF (Laser Induced Fluorescence) thermometry. More than 40 species (reactants, CO, CO₂, H₂O, H₂, and about 14 hydrocarbons as well as 26 oxygenated intermediates up to 5 carbon atoms) were quantified for each doped biofuel flame. The product distributions and consumption pathways of THFA are similar for the 10% and 20% THFA doped flames. The maximum yields of most products increase linearly with the amount of doped THFA. However, some species do not follow this trend indicating interaction chemistry between methane and THFA, which is found to be mainly caused by reaction of the methyl radical. The difference in chemical structure in THFA and MTHF has no notable impact on the mole fractions of CO, CO₂, H₂O, and H₂, but significant differences exist for the yields of intermediates species. The doped THFA flame produces more aldehydes, alcohols, and ethers but it forms clearly less ketones and hydrocarbons. A slightly upgraded version of our previous kinetic model reproduces most experimental data well and it is able to explain the observed differences in intermediate production.

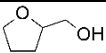
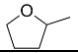
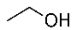
Keywords: Biofuel, THFA, MTHF, premixed flame, gas chromatography, detailed kinetic model

1. Introduction

Even though the share of electric vehicles will rapidly grow and the production of conventional internal combustion engine powered cars will phase out in the next 1-2 decades as announced by major car manufacturers, there will still be a strong need for gasoline and diesel fuels to serve the current fleet of vehicles. In fact, a recent study shows that internal combustion engines will still play a major role in all aspects of road traffic in the near future [1]. The same is true for ships and planes as there is still long haul to electrification of these [2,3]. Advanced biofuels derived from lignocellulosic biomass can play a considerable role in reducing the fossil fuel dependency and the net CO₂ emissions from internal combustion engines [4–8]. Among the biofuels considered [9–18], cyclic ethers of the tetrahydrofuran (THF) family, *e.g.* THF (C₄H₈O), 2-methyltetrahydrofuran (MTHF, C₅H₁₀O), tetrahydrofurfuryl alcohol (THFA, C₅H₁₀O₂), 2,5-dimethyltetrahydrofuran (DMTHF, C₆H₁₂O), and 2-butyltetrahydrofuran (BTHF) have been demonstrated to be accessible from lignocellulosic biomass [15,19–24]. The Lower Heating Values (LHV, ~28-30 MJ/L) of these fuels are higher than that of the most widespread used biofuel today, ethanol (21.3 MJ/L) [16,17,25–28] and close to that of RON95 E10 gasoline (30.8 MJ/L). This means that the driving range with these fuels will be comparable to the commonly used fossil fuels.

Improving the understanding of the combustion chemistry of tetrahydrofuranic fuels is currently a target of intense research around the world [11,29–38]. The present study focuses on two such fuels, namely THFA and MTHF, which have been suggested as biofuel candidates or additives [11]. Table 1 lists relevant physicochemical properties of these fuels such as the RON (Research Octane Number), which indicates the resistance of a fuel towards auto-ignition that is a useful parameter when fuels are used for spark-ignition engines.

Table 1. Relevant physicochemical properties of THFA and MTHF. Those of ethanol and conventional fuels are presented for comparison [9,17,25]. ^a at 298 K. ^bLHV: Lower Heating Value. RON: Research Octane Number.

Fuel	Chemical formula	Structure	Density ^a (kg/L)	Boiling point (K)	LHV ^b (MJ/L)	RON ^b
THFA	C ₅ H ₁₀ O ₂		1.05	451	27.5	--
MTHF	C ₅ H ₁₀ O		0.85	353	28.5	86
Ethanol	C ₂ H ₅ OH		0.80	352	21.3	120
RON95 E10 gasoline	C ₄ -C ₁₄ HC + 10% ethanol		0.74	309-463	30.8	97

Next to the above mentioned favorable LHV compared to that of ethanol, MTHF and THFA are denser liquids than RON95 E10 gasoline (EN51626-1) [9,17,25]. The boiling points of these fuels are in the range of gasoline fuel, however the relatively high boiling point of THFA suggests that this biofuel might preferably be used as a fuel additive.

Besides replacing transportation fuels, biofuels have very recently been proposed to be mixed with natural gas or biogas (mainly methane, CH₄) for clean energy production in dual-fuel combustors (engines or gas turbines) [39,40]. For example, Da Costa et al. [39] studied a dual-fuel engine fueled with two biofuels, biogas and bioethanol. Results show that the dual-fuel mode accelerates the combustion rate when compared to biogas single-fuel operation and improved combustion efficiency. Zheng et al. [40] studied the ignition of dual-fuel mixtures composed of methane with 50% ethanol or propanol and found that ignition delay times of the blend are closer to those of the alcohols than to methane, *i.e.* the ignition delay times are reduced significantly by the added alcohol. Comparable dual-fuel combustion studies with THFA or MTHF as co-fuels are not yet available, meaning that questions concerning the interaction of biofuels with CH₄ and those dealing with optimal biofuel to CH₄ (or natural gas/biogas) ratios are still unanswered.

The use of biofuels as additives in the transportation or power generation sectors requires a sound fundamental understanding of the combustion chemistry of biofuel/fuel mixtures in

order to control the emission of pollutants such as VOCs, aldehydes, ketones, alcohols, etc. These emissions result from incomplete oxidation, hence they contain intermediate products formed during the combustion. Note that the characterization of the toxicological properties of emissions from an engine or a combustor requires the information about the formation of these components [41].

In terms of structure, THFA and MTHF have similar features, but THFA has an additional hydroxyl (OH) group. Thus, a comparative experimental study for these two fuels probes the influence of the OH group on the flame structure and species profiles including toxic ones that might be emitted, while the corresponding simulations provide insight in differences in the dominant kinetics caused by the OH functionality. One objective of the current work is study both fuels at very similar conditions (same burner, analytical equipment, flame conditions) to allow for a straightforward head-to-head comparison, which has not yet been reported in the literature.

The combustion chemistry of MTHF has been investigated extensively [11,30,32,33,36,42–45] and various kinetic models have been reported, such as those by De Bruycker *et al.* [30], Moshhammer *et al.* [32] and Fenard *et al.* [45], whereas the current knowledge of the oxidation chemistry of THFA is limited to the recent investigation by Tran *et al.* [46]. The authors explored the THFA combustion chemistry of a low-pressure burner stabilized 20% THFA/methane flame. Only one fuel mixture (20% THFA) was investigated and numerous intermediate and final products were identified and quantified. A newly developed kinetic model predicted the major products well, and it was concluded that most of the products are formed through THFA specific chemistry. However, the influence of the doped THFA amount and the contributions of interaction chemistry between the two fuels remained unanswered. Note that various levels of interactions through the species pools created by intermediate products have been discussed in the literature and the fuel structure and reaction

conditions are important parameters [47–50]. For example, while Tran *et al.* [48] demonstrated the insignificance of the cross-reactions of primary fuel-specific intermediates of diethyl ether and *n*-pentane in the low-temperature oxidation of their fuel mixtures, Braun-Unkloff *et al.* [47] highlighted the entanglement between the individual fuel-specific species pools in the premixed flames of *n*-heptane/*iso*-butanol mixture. The latter study demonstrated that methyl radicals, mainly from decomposition of *iso*-butanol radicals, were shown to participate in H-abstraction reactions from *n*-heptane. Simultaneously, further interactions were observed in the formation of the methylallyl radical and aromatics.

In line with our previous study on THFA [46], the current study presents, *first*, detailed speciation data for a new 10% THFA/methane premixed burner stabilized flame at the same conditions as used in the previous 20% THFA/methane flame study [46]. Combined with data for a newly measured pure methane flame operated at the same conditions, the impact of different amounts of doped THFA on the chemical flame structure is analyzed. *Second*, a 20% MTHF/methane flame is studied and the results are compared with the 20% THFA/methane flame to explore the effect that replacing the methyl substituent in the alpha position with a hydroxymethyl group has on the combustion chemistry. Since these two flames are operated at the same stoichiometric condition and C/H ratio, this comparison addresses mainly the impact of the OH group in THFA on the flame structure. The kinetic model introduced in [46] with small updates is further validated against the new data sets and then used to explain which reactions cause the differences seen in these flames.

2. Experimental and modelling methods

2.1. Flame conditions

Besides being of interest as a main component of natural gas, methane was chosen as the hydrocarbon base fuel to stabilize the substituted THF flames because the flame chemistry of

CH₄ is well defined and a stoichiometric pure CH₄ flame produces only a small number of light products with no more than three heavy (C, O) atoms. This makes the detection of biofuel specific products easy, which is the focus of the present study. Table 2 summarizes the conditions of the presented flames and introduces the abbreviated names for these flames.

Table 2. Flame conditions. Φ : equivalence ratio. P : pressure. R_{bio} : fraction of doped biofuel in the fuel mixture (=biofuel/(biofuel+CH₄)). Nl/min : normal liter per minute (101.3 kPa, 273.15 K). N₂ (~70%) was used as diluent.

Flame name	R_{bio} (%)	Φ	P (kPa)	Total flow (Nl/min)	Mole fraction of reactants					C/H	C/O	Reference
					N ₂	O ₂	CH ₄	THFA	MTHF			
0% THFA	0	1.0	5.3	5	0.70	0.213	0.107	0	0	0.25	0.25	This study
10% THFA	10	1.0	5.3	5	0.70	0.208	0.077	0.008	0	0.30	0.27	This study
20% THFA	20	1.0	5.3	5	0.70	0.217	0.061	0.015	0	0.34	0.29	[46]
20% MTHF	20	1.0	5.3	5	0.70	0.219	0.059	0	0.014	0.34	0.29	This study

All flames were stabilized on a McKenna flat burner with a diameter of 60 mm at similar conditions: equivalence ratio ($\Phi=1.0$), pressure (5.3 kPa), N₂ dilution (~70%), and total flow (5 Nl/min), thus the same cold gas velocity of 68 cm s⁻¹ (at 333 K and 5.3 kPa). Table 2 shows that the 20% THFA and 20% MTHF flames have the same C/O and C/H ratios, which facilitates a straightforward comparison between those flames. In the 0% to 20% THFA flame series, the C/O and C/H ratios increase with an increasing amount of doping. The overall mass flow rate for the 0% THFA, 10% THFA, 20% THFA, and 20% MTHF flames are 3.63×10^{-3} , 3.72×10^{-3} , 3.81×10^{-3} , and 3.78×10^{-3} g cm⁻² s⁻¹, respectively.

Flow rates of CH₄ (Air Liquide, purity $\geq 99.95\%$), O₂ and N₂ (Air Liquide, purity $\geq 99.995\%$) were controlled using mass flow controllers (Bronkhorst, error $\pm 0.5\%$). The flow rate of the liquid THFA or MTHF (Sigma-Aldrich, purity $\geq 99\%$) was controlled using a Coriolis flow controller (Bronkhorst, error $\pm 0.2\%$) followed by an evaporator/mixer (Bronkhorst), in which THFA or MTHF is evaporated and mixed with N₂. Subsequently, the gaseous stream is mixed with oxygen and CH₄ and fed to the burner housed in a vacuum chamber. The temperature of the burner is kept at 333K using water cooling.

2.2. Temperature measurements and analytical methods

Flame temperature measurements:

Flame temperatures were measured using a combination of NO-LIF (Laser Induced Fluorescence) thermometry and thermocouple without the sampling probe. The details of this technique are available in [51]. A small amount of NO (120 ppm in volume fraction) was added to the nitrogen diluent. This quantity still is sufficiently small to not perturb the chemical structure of the flame as previously proved in [52] but large enough to provide a good signal-to-noise ratio. The laser (Quantel, TDL+ pumped with a seeded YAG Q-smart 850) was tuned over 225.65 – 225.73 nm to excite NO in the A-X(0,0) band. The laser energy was maintained at 40 μ J, which is within the linear LIF regime. The LIF signal was then collected in the A-X(0,2) band of NO using a spectrometer centered at 245 nm. Temperatures were determined through fitting synthetic LIF excitation spectra to the experimental spectra using an automated spectral fitting algorithm named “Thermo NO-LIF” [51,53], with an estimated error ± 100 K in the burned-gas zone. Temperature profiles were complemented by temperatures close to the burner surface (0.25-2 mm above the burner) measured using a commercial K-type thermocouple (250 μ m diameter, TC Direct) with $\sim 1\%$ error. Corrections for radiative heat losses were not applied for the thermocouple measurements because of the temperatures (< 800 K) are low in this region. The reliability of measurements in the zone of overlapping of the two types of technique was tested and an example is presented in Supplemental Material 1 (SM1) (Fig. S1).

Gas chromatograph experiment:

Species mole fraction profiles were measured at the centerline of the flame as a function of height above the burner (h) using a microprobe coupled to gas chromatographs (GCs). Details

of the extraction procedure have been reported previously [34]. Gas samples were extracted from the flame using a quartz probe (250 μm orifice), directed through a heated tube and injected into two GCs. The first GC (Perkin Elmer Clarus 580) was equipped with three columns (Rt-QBond, MS5A, HayeSep Q) and two detectors, *i.e.*, a thermal conductivity detector (TCD) and a flame ionization detector (FID) coupled with a methanizer. CO, CO₂ and formaldehyde cannot directly be detected by FID. The methanizer converts these species to methane which can be detected by FID with a sensitivity higher than that of TCD (by a factor around 100). The second GC (Agilent Technologies 5975C) was equipped with an Rt-QBond column and a mass spectrometer (MS) with electron ionization at 70 eV. The detected species were identified by their MS spectra and their individual GC retention times. Typical chromatograms and MS spectra obtained in the present study are available in SM1 (Fig. S2). Calibration factors were determined using cold-gas mixtures when available. For other species, calibration factors were determined relying on the hydrogenation by the methanizer which converts oxygenates to their corresponding alkanes. This method has been applied successfully in previous studies [34,46]. H₂O mole fractions were calculated independently from both, the H and the O balances, and the average value is reported. The uncertainties of the mole fraction measurements are estimated to be <15% for the most abundant (major) species, <25% for abundant intermediates, and <55% for minor products (<10 ppm). These uncertainties are estimated mainly based on the errors of the mass flow controllers used, of the GC calibration method applied, and the signal-to-noise ratios in the obtained chromatograms. The carbon balance of the flame data was calculated to be 100 \pm 5% (see Fig. S3, SM1), indicating that all important species have been properly identified and quantified.

All flames listed in Table 2 were measured during the same measurement campaign. The used experimental setup and analytical techniques were checked/calibrated before and after the measurement campaign and the change was negligible. Although each species measurement

has its own individual absolute uncertainty, it can be assumed that the uncertainty associated to a given species is similar for all flames measured during this campaign and therefore, a relative comparison of trends between the flames can be performed with significantly higher precision. Indeed, from our two-fold repetition of flame measurements, the repeatability was determined to be <5%.

2.3. Modelling

The studied flames were simulated using the module “Premixed Laminar Burner-Stabilized Flame” of CHEMKIN-Pro 2019R1 package [54] with the inlet gas composition, pressure, and measured temperature profiles provided as input data. The effects of the sampling probe on the flame temperature and species profiles have been discussed in the community intensively and in great detail [55,56]. In line with our previously study [46], the sampling probe slightly affects the position of temperature and species profiles. Therefore, in the present study we moderately shift the temperature profiles in the simulations (0.15 mm for the 20% THFA flame, 0.25 mm for the 10% THFA and 20% MTHF flames) using CH₄ profiles as “maker”. The experimental species profiles presented in figures and provided in SMs are not shifted. Thermal diffusion was included in the simulations and back diffusion at the inlet boundary was allowed. Convergence criteria were decreased until a grid independent solution was found.

A detailed kinetic model for THFA is available from Tran *et al.* [46]. This model was developed based on the MTHF model of De Bruycker *et al.* [30] to which THFA chemistry was added. The MTHF model, in turn, builds on the C₀-C₄ reaction base developed by the Galway group [57,58]. In general, the existing THFA model was able to reproduce the species profiles of the 20% THFA flame well. It is used in the present study with only a few minor updates. These updates are described below. The model construction is summarized in tree form as shown in Fig. S4 (SM1). The updated version is called “*present model*” and if not stated otherwise all simulations discussed in the present paper have been performed using this model.

As mentioned earlier, MTHF kinetic mechanisms have been developed by different groups [30,32,45]. These MTHF mechanisms agree on the major features of MTHF high-temperature chemistry and predictions with these models agree generally well (as shown later in Section 3.2). Therefore, either of these models could be used for MTHF analysis. The MTHF model by De Bruycker *et al.* [30] was selected in the present model without any modifications. Improving the MTHF kinetics is not the scope of the present study which, on the one hand, is concerned with the THFA chemistry including interactions with the co-fuel methane and , on the other hand, with relative differences between the THFA and MTHF flames observed in the present flame data.

The fuel specific chemistry for MTHF and THFA inherent in the “*present model*” was based on ab initio calculations performed at the CBS-QB3 level of theory as previously described in [30,46]. Since the same methodology was used for the sub-mechanisms of both fuels, the relevant reactions are internally consistent. All major reaction classes of the high temperature chemistry of THFA and MTHF, such as unimolecular decomposition, H-atom abstractions by small species (H, CH₃, OH, O, etc.), fuel radical decomposition by ring opening to form acyclic fuel radicals, fuel radical decomposition at the side chain, decomposition of the resulting acyclic fuel radicals from, fuel radical ring enlargement, fuel radical isomerization, oxidation reactions of fuel radicals, and fuel radical-radical disproportionation were included.

Because the previous THFA model reported in [46] cannot well reproduce the mole fraction profiles of 4-pentenal (4C₄H₇CHO) and *n*-butanal (nC₃H₇CHO), which are two important intermediates measured in the doped THFA flames. The former species was overpredicted, while the latter species was underpredicted. To address these shortcomings the following changes were made: First, the reaction subset of nC₃H₇CHO (both rate coefficients and thermochemical properties) proposed in [59] was implemented into the model without any changes. Second, it was found that important consumption reactions for 4C₄H₇CHO were

missing and had to be added. Fig. 1 presents these reactions, which include the retroene reaction (i) and H- and OH-additions to the double bond ((ii) and (iii)). The rate coefficients (Table 3) of (i) were calculated in the present study at the CBS-QB3 level of theory using the same procedure as outlined in [46], while those proposed in [60] have been used for (ii) and for the first path of (iii). The first pathway of (ii) and the second pathway of (iii) were already available from [46] but is presented in Fig. 1 to provide an overview of the OH-addition processes. These changes lead to improved predictions of the $n\text{C}_3\text{H}_7\text{CHO}$ and $4\text{C}_4\text{H}_7\text{CHO}$ profiles (see Fig. S5, SM1).

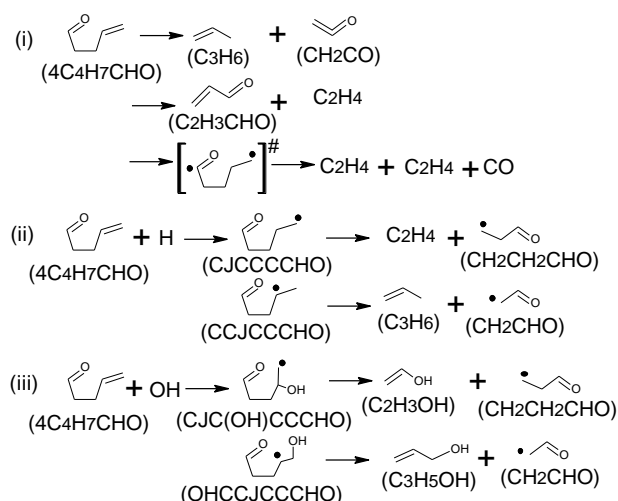


Fig. 1. New reactions added for 4-pentenal ($4\text{C}_4\text{H}_7\text{CHO}$): (i) Retroene reaction and H migration, (ii) H-additions, (iii) OH-additions. The rate coefficients of these reactions are summarized in Table 3.

Table 3. Rate coefficients of the newly added reactions for 4-pentenal ($4\text{C}_4\text{H}_7\text{CHO}$), *i.e.* those in Fig. 1. The rate coefficients ($k = AT^n \exp(-E_a/RT)$) are given in cm^3 , mol, s, cal units.

Reactions	A	n	E_a	Reference
(i) Retroene reaction and H migration:				
$4\text{C}_4\text{H}_7\text{CHO} \rightleftharpoons \text{C}_3\text{H}_6 + \text{CH}_2\text{CO}$	3.90E+05	1.53	6.39E+04	This study
$4\text{C}_4\text{H}_7\text{CHO} \rightleftharpoons \text{C}_2\text{H}_3\text{CHO} + \text{C}_2\text{H}_4$	2.20E+09	1.14	6.58E+04	This study
$4\text{C}_4\text{H}_7\text{CHO} \Rightarrow \text{C}_2\text{H}_4 + \text{C}_2\text{H}_4 + \text{CO}$	2.30E+06	1.67	5.60E+04	This study
(ii) H-additions:				
$4\text{C}_4\text{H}_7\text{CHO} + \text{H} \rightleftharpoons \text{CJCCCCHO}$	6.46E+13	0.00	5.38E+03	[60]
$\text{CJCCCCHO} \rightleftharpoons \text{C}_2\text{H}_4 + \text{CH}_2\text{CH}_2\text{CHO}$	2.00E+11	0.66	2.86E+04	[46]
$4\text{C}_4\text{H}_7\text{CHO} + \text{H} \rightleftharpoons \text{CCJCCCHO}$	5.56E+13	0.00	3.85E+03	[60]
$\text{CCJCCCHO} \rightleftharpoons \text{C}_3\text{H}_6 + \text{CH}_2\text{CHO}$	2.07E+13	0.00	2.28E+04	[60]
(iii) OH-additions:				
$4\text{C}_4\text{H}_7\text{CHO} + \text{OH} \rightleftharpoons \text{CJC(OH)CCCHO}$	1.56E+08	1.29	-2.65E+03	[60]
$\text{CJC(OH)CCCHO} \rightleftharpoons \text{C}_2\text{H}_3\text{OH} + \text{CH}_2\text{CH}_2\text{CHO}$	4.41E+13	0.00	2.75E+04	[60]
$\text{HOCCJCCCHO} \rightleftharpoons \text{OH} + 4\text{C}_4\text{H}_7\text{CHO}$	1.40E+16	-1.01	2.85E+04	[46]
$\text{HOCCJCCCHO} \rightleftharpoons \text{C}_3\text{H}_5\text{OH} + \text{CH}_2\text{CHO}$	3.62E+09	0.97	2.04E+04	[46]

Since the present study is concerned with dual-fuel flames (THFA or MTHF doped CH₄ flames), it is important to ensure that potentially important cross-reactions between the fuels and/or their corresponding radical pools are included in the model. It is assumed that this interaction chemistry is dominantly initiated through H-abstraction reactions by radicals produced from the fuel molecules. H-abstraction reactions from THFA and MTHF were already incorporated in the original THFA model, however, some additional H-abstraction reactions from CH₄ by THFA or MTHF derived radicals were missing and have been added with rate coefficients being estimated based on rate rules [61] (Table S1). The main possible cross-reaction routes are summarized in Fig. S6 (SM1).

The final kinetic model consists of 2978 reversible reactions involving 487 species and available in CHEMKIN format in SM2. Here, the IUPAC International Chemical Identifier (InChI) is provided for each species, which allows to unambiguously identify the molecular structure. Compared to the previous model [46], the present model contains only three new species (CCJCCCHO, CJC(OH)CCCHO, CC(=O)COH, see structures in Table S2), which result from new reactions shown either in Fig. 1 or in Table S1. The thermochemical data of these three species were taken from [60–62], respectively. For consistency with the employed rate coefficients, the thermochemical data of nC₃H₇CHO is taken from [59], while those of other species in the model are those of the previous (original) model [46].

3. Results and discussions

First, the combustion chemistry of THFA is presented in Section 3.1. Here the chemical structure of the 10% THFA flame is discussed in Sections 3.1.1 and 3.1.2. The impact of the different doped THFA amounts (0%, 10%, 20%) and the contribution of THFA to the formation of common products are analyzed in Sections 3.1.3 and 3.1.4. Second, the 20% MTHF flame is presented and compared with the 20% THFA flame in Sections 3.2. Because the combustion chemistry of MTHF is well understood, the species profiles measured in the 20% MTHF flame

are only briefly summarized in Sections 3.2.1 and 3.2.2 to serve as a base for the comparative analyses with THFA in Sections 3.2.3 and 3.2.4. Two ordering systems, by heavy atom number (Section 3.1) or by chemical family (Section 3.2) are used in the manuscript. The former is useful for exploring the biofuel primary chemistry (taking advantage of the fact that the methane flame produces only intermediates and products with 3 or less heavy atoms), the latter is more suitable for the discussion of emissions by the two biofuels.

3.1. THFA flame chemistry in doped methane flames

In this section, the new 10% THFA flame data are presented and compared to the 20% THFA flame results studied by Tran *et al.* [46], with the aim to further explore the flame chemistry of THFA in the mixed fuel flames. Prior to comparison to the 20% THFA flame, the 10% THFA flame is analyzed (Sections 3.1.1 and 3.1.2) to examine THFA combustion behavior for a lower degree of THFA doping. The impact of the degree of doping on the flame structure and species profiles are analyzed (Sections 3.1.3 and 3.1.4).

3.1.1. Fuel, final products, and temperature profiles of the 10% THFA flame

The consumption profiles of the inlet species, flame temperature, and the formation of the major final products are shown in Fig. 2 and compared to the model predictions. In general, the measurements and the predictions agree well. As expected, CO₂ and H₂O are predominant in the burned gas because of the studied conditions, but small fractions of O₂ and CO remain present in the post flame zone because chemical equilibrium is not yet reached. Fig. 2 also includes the data reported in [46] for the 20% THFA flame. The trends follow largely the expectations in the sense that the concentration profiles are very similar. Nevertheless, small differences are seen which indicate that the reactivity of the higher doped flame is slightly higher. This can be seen from the faster temperature increase, the slightly faster consumption of THFA, CH₄ and oxygen and the early formation of CO and CO₂. This observation suggests that THFA has a higher laminar burning velocity compared to methane.

It can be observed that the final temperature reached by the 20% THFA flame is slightly higher (~ 100 K) than that of the 10% THFA flame possibly due to the higher heat of combustion of THFA (2961 kJ/mol vs 891 kJ/mol for CH_4). However, this difference in temperature is still in the range of experiment uncertainty declared in Section 2.2.

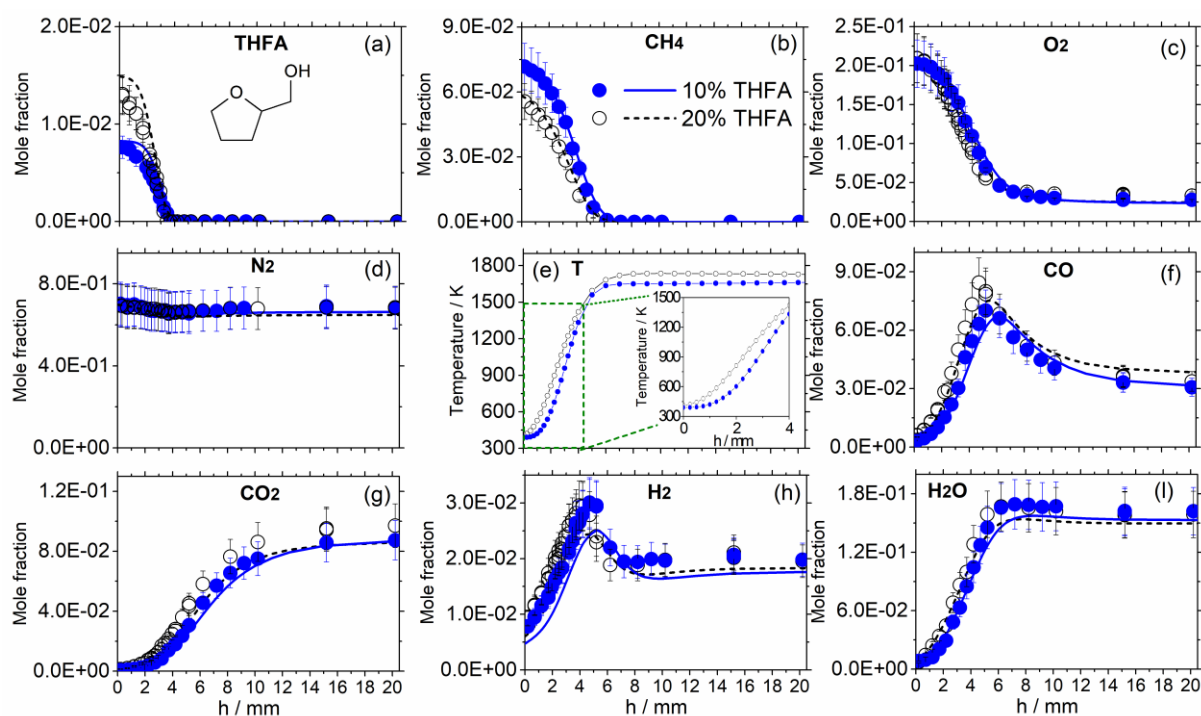


Fig. 2. Comparison of the mole fraction profiles of major species obtained in the 10% and 20% THFA flames: reactants (THFA, CH_4 , O_2) (a-c), diluent (N_2) (d), temperature (T) (e) and main products (CO_2 , CO , H_2 , H_2O) (f-i). Symbols: experimental data (see initial conditions in Table 2), lines: present model. The experimental data of the 20% THFA flame is taken from [46]. Error bars in this and following figures are based on the uncertainties discussed in Section 2.2.

3.1.2. Intermediate products of the 10% THFA flame

Experimentally measured C_1 - C_5 intermediate species (12 hydrocarbons, 22 oxygenates) of the 10% THFA flame are summarized in Table 4. The name, nomenclature, structure and peak mole fraction of these intermediate species are included. Mole fraction profiles with model predictions for important intermediate species are presented in Fig. 3, those for other species are available in SM1 (Fig. S7). The employed GC setup allowed to distinguish between several different isomers, *e.g.* two different C_3H_4 species were detected, four $\text{C}_3\text{H}_6\text{O}$ intermediates and

four species with the same formula C_4H_6O (see more details in Table 4). Also, hydrocarbons and oxygenated species with the same nominal mass, *e.g.* six species at mass 58 and five species at mass 70 (Table 4) could be separated. Although absolute values are obviously different, the relative species composition of the 10% THFA flame is very similar to that observed previously for the 20% THFA flame [46]. Therefore, we present only selected species profiles here. The entire set of species data can be found in SM3.

Table 4. Intermediates measured in the 10% THFA flame. *SG*: species group based on the number of heavy atoms (C and O). *M*: nominal mass (g/mol). x_{max} : peak mole fraction. *CPaldehyde*: Cyclopropanecarboxaldehyde. *THFAldehyde*: Tetrahydrofuran-2-aldehyde. **Bold**: highlighting the most abundant species in its respective SG. **Bold Italic**: highlighting the next two abundant species (within a factor 3 compared to the highest one, except for furan).

SG	Formula	Nomenclature	M	Name	Structure	x_{max}
Group 1: Two heavy atoms	C ₂ H ₂	C ₂ H ₂	26	Acetylene		9.02E-04
	C₂H₄	C₂H₄	28	Ethylene		3.08E-03
	C₂H₆	C₂H₆	30	Ethane		1.50E-03
	CH₂O	CH₂O	30	Formaldehyde		2.14E-03
	CH ₄ O	CH ₃ OH	32	Methanol		1.92E-04
Group 2: Three heavy atoms	C ₃ H ₄	aC ₃ H ₄	40	Allene		5.92E-06
	C ₃ H ₄	pC ₃ H ₄	40	Propyne		1.18E-05
	C₃H₆	C₃H₆	42	Propene		3.76E-04
	C₃H₈	C₃H₈	44	Propane		1.35E-04
	C₂H₄O	CH₃CHO	44	Acetaldehyde		2.43E-04
	C ₂ H ₆ O	C ₂ H ₅ OH	46	Ethanol		6.40E-06
	C ₂ H ₆ O	CH ₃ OCH ₃	46	Diethyl ether		2.71E-05
Group 3: Four heavy atoms	C ₄ H ₆	1,3C ₄ H ₆	54	1,3-Butadiene		1.70E-05
	C ₄ H ₈	1C ₄ H ₈	56	1-Butene		3.43E-05
	C ₄ H ₈	2C ₄ H ₈	56	2-Butene		2.81E-06
	C₃H₄O	C₂H₃CHO	56	Acrolein		9.74E-05
	C ₄ H ₁₀	iC ₄ H ₁₀	58	iso-Butane		2.60E-06
	C ₄ H ₁₀	nC ₄ H ₁₀	58	n-Butane		4.26E-05
	C ₃ H ₆ O	CH ₃ COCH ₃	58	Acetone		1.44E-05
	C₃H₆O	C₂H₅CHO	58	Propanal		9.32E-05
	C₃H₆O	C₃H₅OH	58	Allyl alcohol		1.36E-04
	C ₃ H ₆ O	C ₃ H ₆ O1,2	58	Propylene oxide		3.18E-06
Group 4: Five heavy atoms	C₄H₄O	Furan	68	Furan		1.23E-05
	C ₅ H ₁₀	1C ₅ H ₁₀	70	1-Pentene		1.25E-06
	C₄H₆O	2,3DHF	70	2,3-Dihydrofuran		7.02E-05
	C ₄ H ₆ O	cyC ₃ H ₅ CHO	70	CPaldehyde		3.47E-06
	C ₄ H ₆ O	sC ₃ H ₅ CHO	70	2-Butenal		8.62E-06
	C ₄ H ₆ O	MVK	70	Methyl vinyl ketone		1.15E-06
	C ₄ H ₈ O	C ₂ H ₅ COCH ₃	72	Butanone		1.06E-05
	C₄H₈O	nC₃H₇CHO	72	Butanal		3.28E-05
Group 5: Six-seven heavy atoms	C₅H₈O	3,4DHP	84	3,4-Dihydro-2H-pyran		2.74E-05
	C₅H₈O	4C₄H₇CHO	84	4-Pentenal		1.49E-05
	C ₅ H ₁₀ O	nC ₄ H ₉ CHO	86	n-Pentanal		1.41E-06
	C ₅ H ₁₀ O	C ₃ H ₇ COCH ₃	86	2-Pentanone		1.79E-06
	C₅H₈O₂	THFCHO	100	THFAldehyde		1.87E-05

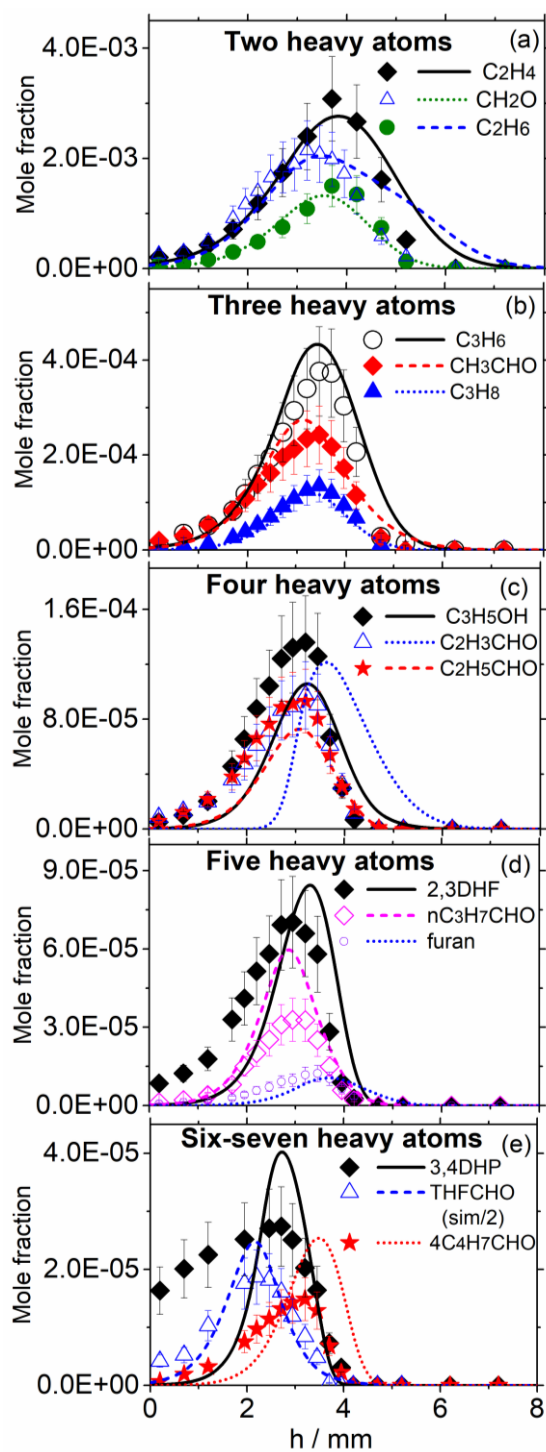


Fig. 3. Mole fraction profiles as a function of the height above the burner (h) of the most important intermediate species measured in the 10% THFA flame. *Symbols*: experimental data with estimated error bars (see initial conditions in Table 2), *lines*: present model.

The detected intermediates are classified in five groups based on the number of heavy atoms (C and O) (Table 4).

The **group 1 (two heavy atoms)** includes three C_2H_x and two CH_xO species with C_2H_4 being the most abundant species followed by C_2H_6 and CH_2O . The model predicts the profiles

of these species well (Fig. 3a).

The **group 2 (three heavy atoms)** includes four C_3H_x and three C_2H_xO species. C_3H_6 is the most predominant intermediate followed by C_3H_8 and CH_3CHO . Again, the model predicts the formation of these species well (Fig. 3b).

The **group 3 (four heavy atoms)** composes of five C_4H_x and five C_3H_xO species. Clearly the oxygenated species, *i.e.*, C_3H_5OH , C_2H_5CHO and C_2H_3CHO dominate. Fig. 3c shows that the model over-predicts C_2H_3CHO by 24% and under-predicts C_3H_5OH and C_2H_5CHO by 23%. These deviations are, however, within the experimental uncertainties (Section 2.2). The predicted profiles are also slightly shifted towards higher burner heights indicating that the overall formation chemistry included in the model for these species is slightly slower than that observed experimentally.

The **group 4 (five heavy atoms)** contains almost entirely oxygenated species (seven C_4H_xO species) with 1-pentene ($1C_5H_{10}$) as exception. 2,3DHF and nC_3H_7CHO are detected with the highest mole fractions. The next important species is furan. Fig. 3d shows that although the model slightly over-predicts the nC_3H_7CHO yield, it predicts the order of these species correctly.

The **group 5 (six and more heavy atoms)** includes five C_5H_xO species but no pure hydrocarbon. The six-membered ring species 3,4DHP is detected with the highest mole fraction, followed by THFCHO and $4C_4H_7CHO$. nC_4H_9CHO and $C_3H_7COCH_3$ were measured with very low mole fractions. The model over-predicts the peak mole fraction of THFCHO by a factor of two but the shape and location of the profile are well reproduced (Fig. 3e). Although the model cannot reproduce the shape of 3,4DHP profile in the zone near the burner surface, the predicted and experimental peak values are in reasonably good agreement. Looking at its mole fraction profile, 3,4DHP might appear to be an impurity in THFA. However, the THFA sample used in these experiments was analyzed by GC and 3,4DHP was not detected. If

formation paths of 3,4DHP were missing in the gas phase model, this reaction needs to be highly effective in the region close to the burner surface and at the same time cannot have a notable impact at later states, where the 3,4DHP profile is well predicted. At this moment, the appearance of 3,4DHP close to the burner surface cannot be convincingly explained. The peak value of $4C_4H_7CHO$ is well simulated and the model also captures the shift of the profile towards higher heights above burner compared to THFCHO.

3.1.3. Impact of the degree of doping on the flame structure

A comparison for the temperature, fuel and final product profiles of the 10% THFA and 20% THFA was already presented above (Fig. 2). In this section, the yields of intermediate species found in both flames are compared and related to the pure methane flame. Figure 4 presents the (normalized) experimental peak mole fractions for 35 intermediate species containing between 2 and 7 heavy atoms.

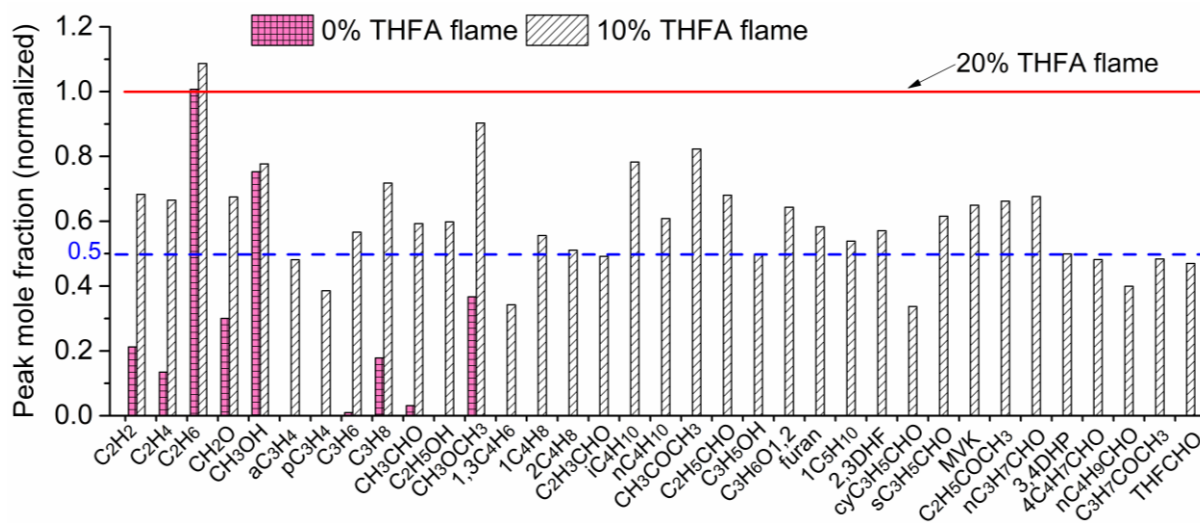


Fig. 4. Comparison of (normalized) experimental peak mole fraction of the three studied flames. Normalization was performed using the data of the 20% THFA flame as reference. For clarity, peaks of individual species of the 20% THFA flame are not shown but indicated as the horizontal red solid line. The experimental data of the 20% THFA flame is taken from [46]. Initial conditions are available in Table 2.

Except for C_2H_6 , the highest peak mole fractions are found in the 20% THFA flame. The pure methane flame (0% THFA doping) contains only a small number of intermediate species with molecular weights not exceeding 46 (C_2H_6O). aC_3H_4 , pC_3H_4 , C_2H_5OH , and heavier species

(mass > 46) are not present in measurable amounts in the undoped flame. Figure 4 also shows that the peak mole fractions generally increase significantly when going from the 10% to the 20% doped THFA flame – often the increase seems roughly proportional to the amount of available THFA.

This trend reflects that these species are dominantly produced from THFA and are THFA-specific intermediates. A rate analysis for the 20% THFA flame presented in [46] demonstrated the pathways for many of these intermediates and a similar analysis for the 10% THFA flame is discussed below.

Species commonly detected in the three flames are C_2H_x ($x=2, 4, 6$), CH_2O , CH_3OH , C_3H_6 , C_3H_8 , CH_3CHO , and CH_3OCH_3 . Among these, the peak values for C_2H_6 , CH_3OH and to lesser degrees CH_3OCH_3 stand out. They are produced in large amounts in all three flames. The formation of these species depends on the availability of CH_3 radicals which are abundantly present in all flames, because CH_3 radicals are largely produced from methane. A slightly higher peak mole fraction of C_2H_6 is observed in the 10% THFA flame compared to the 20% THFA flame, but both peak yields agree within the experimental uncertainty. The relative yields of iC_4H_{10} and CH_3COCH_3 are also higher than 50% in the 10% THFA flame. The formation of these species also requires a CH_3 radical since they are produced via reactions of this radical with the three-heavy-atom radicals, iC_3H_7 and CH_3CO , respectively. $1,3C_4H_6$ and cyC_3H_5CHO yields are relatively low in the 10% THFA flame compared to half of the 20% THFA flame, but these differences are again still within the expected uncertainty.

Figure 5 presents a comparison of experimental and modelling mole fraction profiles of the most significant species for each species group in the two doped THFA flames (10% and 20% THFA). Overall, the model predicts the trends and the absolute mole fractions of the species well, even though some non-negligible discrepancies between the model and experiments exist. For example, in the case of C_3H_8 , the model predicts approximately similar

yields for both fuels while the experimental yields increase with the amount of THFA. For nC_3H_7CHO , the trends are reversed; the model predicts less butanal in the 20% THFA flame than in the 10% doped flame. The same reversal is seen for THFCHO. On the other hand, the orders in peak yields are correctly reproduced for CH_2O , C_2H_3CHO , C_2H_5CHO , and $4C_4H_7CHO$. Since the experimental data seem to be internally consistent, the deviations point to weaknesses of the kinetic model.

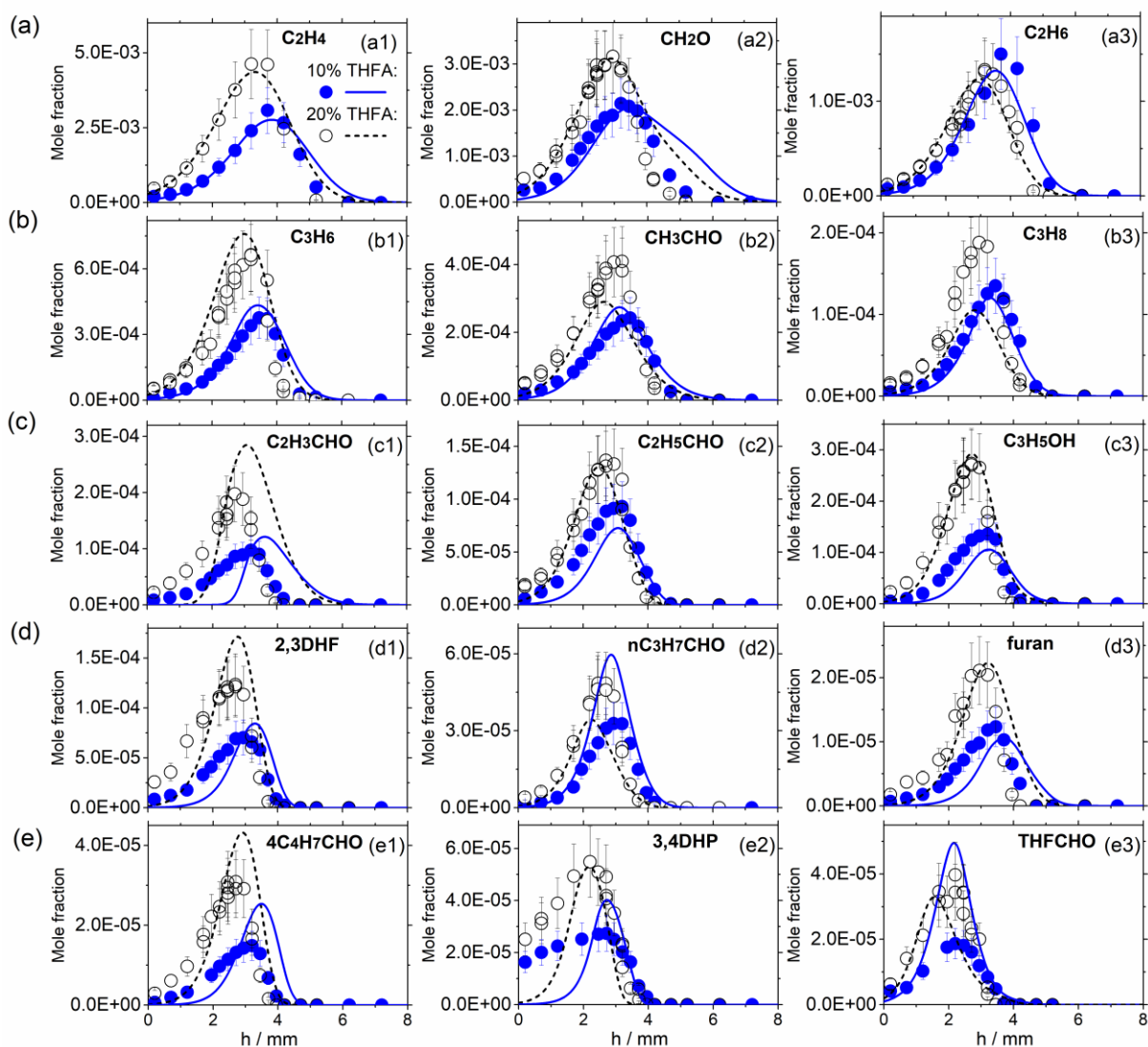


Fig. 5. Comparison of mole fraction profiles of selected *fuel-specific decomposition* products of the 10% and 20% THFA flames. Species presented are those highlighted in **bold** font in Table 4, *i.e.*, the most abundant species of each species group, respectively. **(a), (b), (c), (d), (e)**: two, three, four, five, six-seven heavy atom group, respectively. *Symbols*: experiment (see initial conditions in Table 2), *lines*: present model. The experimental data of the 20% THFA flame is taken from [46].

The important pathways of THFA in the two flames (10% and 20% THFA) are analyzed using the present model. It is interesting that the result is very similar meaning that the rate analysis for the 20% THFA doped flame holds for the 10% THFA flame. This is reasonable since the important initial pathways (once H-abstraction occurred) are unimolecular processes and thus they are concentration independent. Furthermore, as can be seen in Fig. 2, THFA decomposes faster than methane, hence the impact of interaction chemistry on the consumption of THFA is limited to a few product channels. The reader is referred to Fig. S8 of SM1 and to Ref. [46] for further details.

3.1.4. Contribution of THFA to the formation of the low molecular weight products

An attempt has been made to dissect the contributions of both fuels (methane and THFA) to the formation of common products through simulations with the current kinetic model. The idea is to run the model twice, once with both fuels (THFA and CH₄) being reactive species and a second time at the same conditions but making THFA nonreactive. To implement this idea, an inert fictitious THFA species (namely *F-THFA*) was introduced into the model, which is based on the literature approach [63,64]. The thermochemical and transport data for F-THFA are the same as for THFA which ensures that the energy balance and transport properties remains the same, but F-THFA does not participate in any chemical reactions. In addition, to keep the equivalence ratio of the doped F-THFA flames the same as that of the doped THFA flames, a part of oxygen was replaced by inert fictitious O₂ (written as F-O₂). F-O₂ again has exactly the same thermochemical and transport properties as well as third-body collision efficiencies as normal O₂ but is chemically inert. The conditions of the doped fictitious-THFA flames are summarized in Table 5.

Table 5. Conditions of the doped F-THFA flames. ^a Based on CH₄ and O₂.

Flame name	R _{bio} (%)	Φ ^a	P (kPa)	V (cm/s)	Mole fraction				
					N ₂	O ₂	F-O ₂	CH ₄	F-THFA
10% F-THFA	10	1	5.3	68	0.7	0.154	0.054	0.077	0.008
20% F-THFA	20	1	5.3	68	0.7	0.121	0.096	0.061	0.015

When replacing THFA by F-THFA in flame simulations, combustion products are not formed from THFA, but originate entirely from CH₄ reactions. The contribution of THFA to the formation of products is taken as the difference between the doped THFA flames and the doped F-THFA flames (see Fig. 6a). It may not be a perfect method for such analysis, but this method should provide some indications regarding the participation of individual fuels in the formation of common products. Thus, this analysis aims to contribute to the understanding of the combustion chemistry of THFA. The simulations were performed using the same procedure as described in Section 2.3. Selected results of this analysis are presented in Fig. 6b,c. The contribution of THFA to CO and CO₂ formation is approximately linearly proportional to the amount of carbon supplied by THFA (34% and 55%, in the 10% and 20% THFA flames, respectively). For example, in the 20% THFA flame, the THFA fraction contributes to 55% of the total carbon and the above analysis shows that 50% CO and 54% CO₂ originates from THFA reactions. Similarly, the contribution of THFA to the H₂ and H₂O formation increases linearly with the THFA fraction that supplies 21% and 38% H as well as 2% and 3% O to the 10% and 20% THFA flames, respectively. However, the contribution of THFA to the formation of intermediate species is not always linearly proportional to the added THFA amounts, which depends strongly on the structure of these species (Fig. 6c). For example, THFA contributes only a small part to the formation of C₂H₆, which is consistent with the observed insignificant influence of the doped THFA fraction on this species in Section 3.1.3, while THFA contributes notably to the formation of C₃H₆ and CH₃CHO (93-99%) when THFA is added either 10% or 20%. This latter trend indicates that these products are mainly produced through the main consumption routes of THFA and hardly from CH₄. This conclusion is in agreement with the

experimental data shown in Fig. 4 and the model analysis presented in Fig. S8. The results from this fictitious THFA analysis are consistent with the experimental data discussed above.

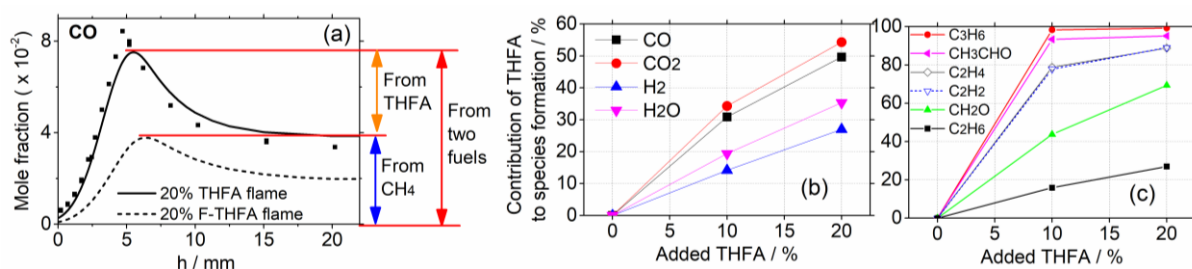


Fig. 6. Contribution of the individual fuel to the formation of combustion products. **(a)** Explanation how the contribution is calculated. *Symbols*: experiment. *Lines*: present model. **(b,c)** Selected simulation results. Initial conditions are available in Table 2 and Table 5.

3.2. The 20% MTHF flame structure and its comparison with the 20% THFA flame

The objective of this section is to reveal the influence of the chemical structure of the two biofuels on their combustion behavior and the formation of products. Prior to using them in the comparative study with THFA, the results of the 20% MTHF flame are analyzed with an aim to understand MTHF combustion behavior in the similar fuel mixture flame.

In the following sections, first, the reactants and the final product profiles are presented (Section 3.2.1). Afterwards, the intermediate products measured in the 20% MTHF flame are discussed (Section 3.2.2) and compared to those detected in the corresponding 20% THFA flame (Sections 3.2.3 and 3.2.4). With the help of a reaction pathway analysis for the 20% MTHF flame the differences between both flames are explained (Section 3.2.4).

3.2.1. Fuel consumption and final products

Figure 7 compares the measured mole fraction profiles of fuels (THFA, MTHF, CH₄) (a), O₂ (b), and the final products (CO, CO₂, H₂, H₂O) (c-f) in the 20% MTHF and 20% THFA flames. The mole fraction profiles of these final products are very similar for the two flames. The model reproduces these observations. The similarities at higher heights above the burner reflect the constant C/O and C/H ratios of the two flames (Table 2) while the essentially equal profile shapes at low heights above the burner point to comparable reactivities or flame speeds of both

fuels. Veloo *et al.* [65] pointed out that saturated C_{2+} alcohols have quite similar flame speeds compared to their alkane counterparts. The close similarity of the profiles of THFA and MTHF (Fig. 7) indicates that these biofuels follow this trend.

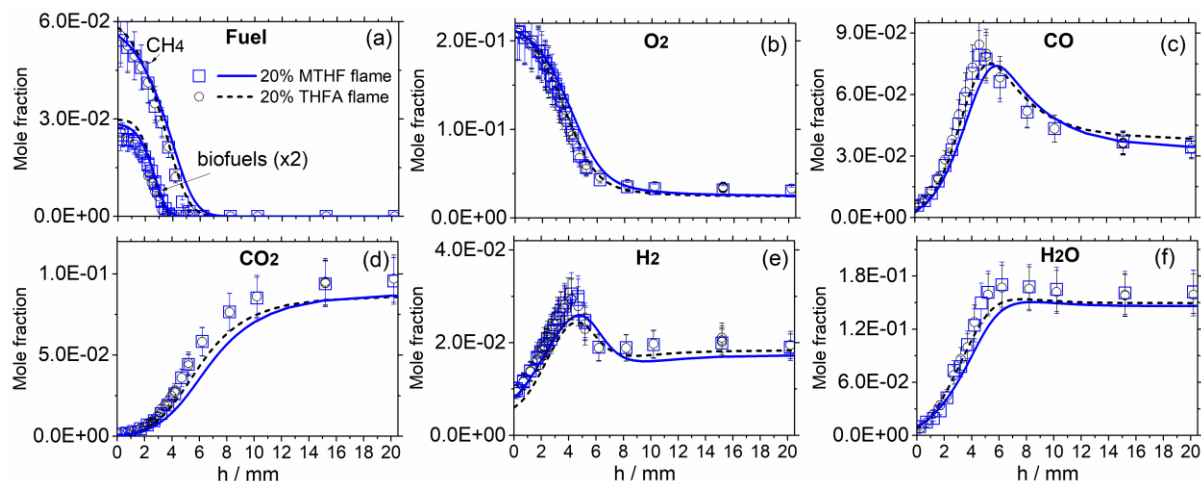


Fig. 7. 20% THFA vs 20% MTHF flames: Mole fractions of the reactants and the major final products.

Symbols: experiments (see initial conditions in Table 2), *lines:* present model. For clarity, the experimental and simulated profiles of biofuels (THFA and MTHF) were multiplied by a factor of 2. The experimental data of the 20% THFA flame is taken from [46].

3.2.2. Intermediate products

A selected set of important intermediates formed in the 20% MTHF flame are shown in Fig. 8. The complete set of experimental profiles of the intermediate products can be found in SM3. Species names and structures are available in Table S3 (SM1). Figure 8 also contains modeling results with the present and two alternative MTHF models [32,45]. Simulations with the model by [43] were not performed because the transport data file was not provided in [43].

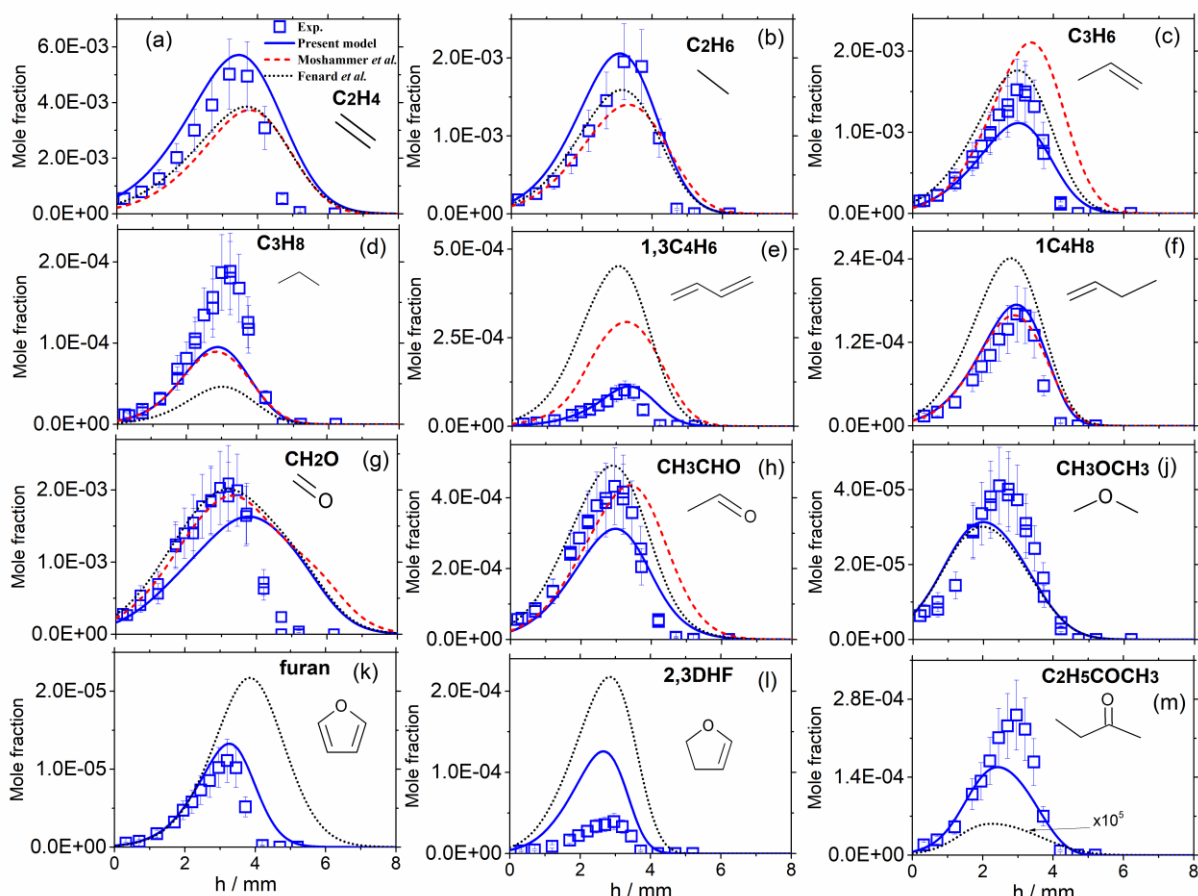


Fig. 8. Mole fraction profiles of selected intermediate species detected in the MTHF flame. *Symbols:* experiment (see initial conditions in Table 2), *lines:* three available MTHF models (*Solid line:* present model. *Dashed lines:* model of Moshammer *et al.* [32]. *Dotted lines:* model of Fenard *et al.* [45]). CH_3OCH_3 , furan, 2,3DHF, and $\text{C}_2\text{H}_5\text{COCH}_3$ are not present in the model of [32].

C_2H_4 was measured with the highest mole fraction. C_2H_6 , C_3H_6 , C_3H_8 , 1,3- C_4H_6 , and $1\text{C}_4\text{H}_8$ are also abundant C_2 - C_4 hydrocarbon intermediates. Overall, the three models successfully reproduce the profiles of these species although some discrepancies exist for C_3H_8 and 1,3 C_4H_6 . CH_2O and to a lesser degree CH_3CHO are also present with high peak concentrations and the models capture the peak concentrations well even though the present model slightly underpredicts the CH_2O yield and predicts the CH_2O profile to be broader than measured. CH_3OCH_3 is an abundant ether intermediate and reasonably well predicted by the present and Fenard *et al.* [45] models. The furanic species are the next abundant ethers. The previously mentioned two models also fare well for furan but overpredict the formation of

2,3DHF, which according to the models is exclusively produced via C_{ring}-C_{lateral} bond of the MTHF3J radical. C₂H₅COCH₃ was experimentally identified as the most abundant one among the 6 quantified ketones. The present model underpredicts its peak concentration by about 40%, but still performs quantitatively better than other models.

In summary, there are clearly some discrepancies that may need further refinements in the MTHF mechanisms, *e.g.* 2,3DHF and C₂H₅COCH₃ formation, especially considering the newly reported flame data. However, the major species (see Fig. 7 for the present model; the models of [32,45] achieve similarly good agreements) and the selected intermediates shown in Fig. 8 are overall satisfactorily reproduced, indicating that the most important chemistry is well understood and incorporated in these models.

3.2.3. Comparison of the 20% MTHF and 20% THFA flames

Chemical species classified as intermediates in combustion studies have been detected in the exhaust gas of technical engines, as recently demonstrated by [66] for 2,5-dimethylfuran. Therefore, a comparison of the quantified intermediates from THFA and MTHF, as presented in the following paragraphs, is expected to be useful not only to support the analysis of the combustion chemistry but also to indicate which exhaust species might be expected. These possible exhaust species provide a first guess of the toxicological properties of engine emissions powered by a given fuel. In general, among the detected intermediates, formaldehyde, acetaldehyde, methanol and allyl alcohol are known to be highly toxic.

In Fig. 9, the intermediate products formed in the 20% MTHF and 20% THFA flames are compared. Part (a) presents relative yields of all detected intermediates as bar diagram and part (b) condenses the data in species groups and marks in bold letters the most abundant species of that group.

While the overall reactivity and yields of final products was seen to be very similar for the two flames (Section 3.2.1), Fig. 9 shows clear differences in the intermediate distributions.

Several species, 1,3-pentadiene ($1,3C_5H_8$), two ketones ($cyC_3H_5COCH_3$, $sC_3H_5COCH_3$; their structures are given in the bottom panel), 4-pentenol ($4C_5H_9OH$) and 5-methyl-2,3-dihydrofuran (MDHF) have only been detected in the 20% MTHF flame, while some aldehydes (cyC_3H_5CHO , nC_4H_9CHO , $THFCHO$) and 3,4DHP were only found in the 20% THFA flame. In general, the 20% MTHF flame produces larger amounts of hydrocarbon intermediates and ketones while most aldehydes are preferentially formed in the 20% THFA flame. Each species family is discussed below. Note that absolute peak mole fractions for the two biofuels are also available in Table S3 (SM1) in which species are classified by chemical family facilitating the examination of the potential of pollutant emissions (carbonyl components, soot precursors, ect.). Acids were not detected in the studied flames.

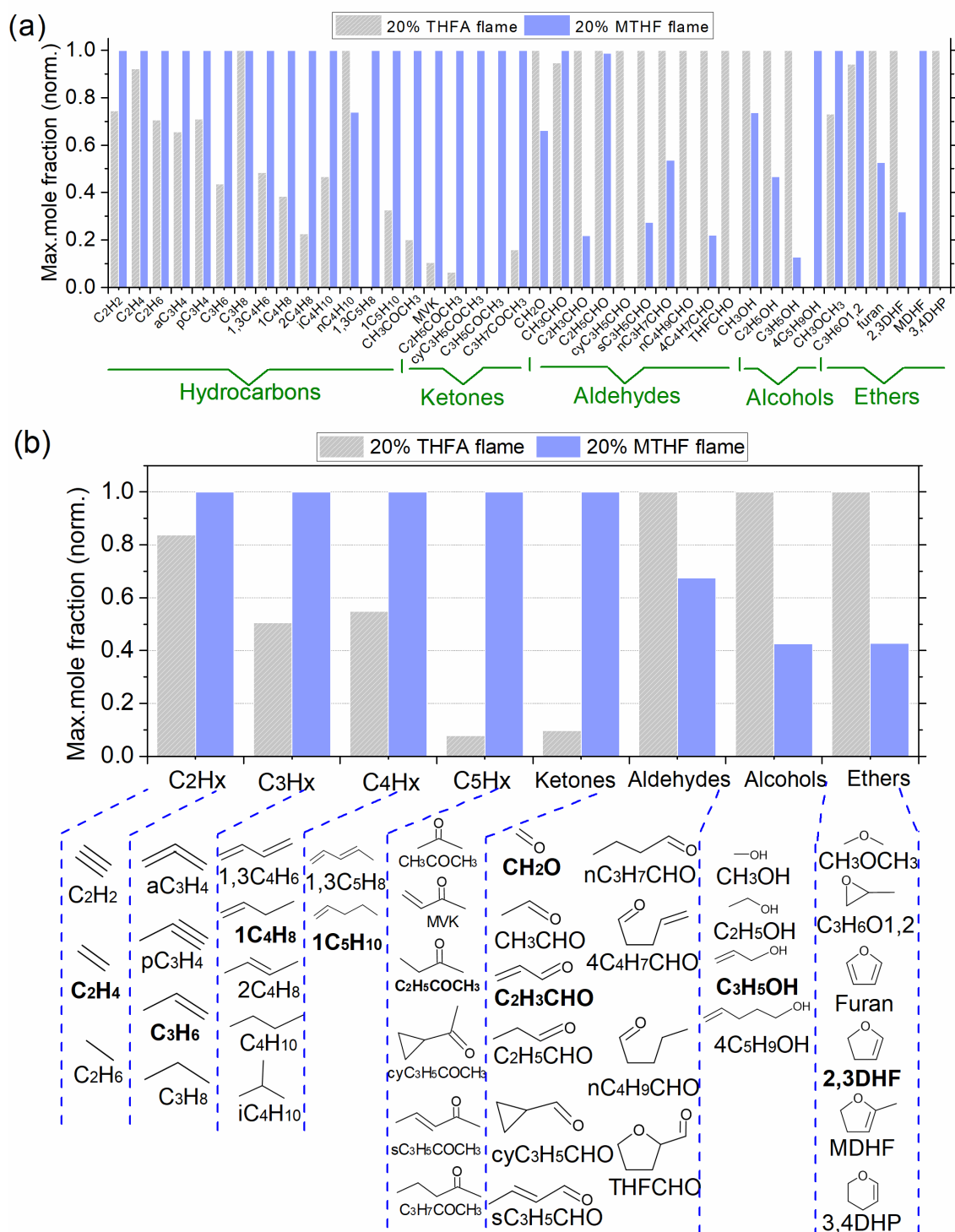


Fig. 9. Comparison of (normalized) experimental peak mole fraction between the 20% THFA and 20% MTHF flames (initial conditions in Table 2). (a) All intermediate species. (b) Sum of species in their respective family.

Species highlighted in **bold** are those having the largest impact on the difference of the total amount of the respective species family. The experimental data of the 20% THFA flame is taken from [46].

Hydrocarbons: The total amount of the measured hydrocarbons is higher in the 20% MTHF flame (Fig. 9b). Except for C₃H₈ and nC₄H₁₀, the 20% MTHF flame produces all

hydrocarbons in higher quantities than the 20% THFA flame (Fig. 9a, Table S3 (SM1)). The yield differences are relatively small for the C_2 species (Fig. 9b), but those for C_3 and C_4 species exceed a factor of two and are even more significant for C_5 species. Because of the high mole fractions, C_2H_4 , C_3H_6 , $1C_4H_8$, and $1C_5H_{10}$ control the observed differences in the total amounts of C_2 , C_3 , C_4 , and C_5 , respectively. The present model predicts the relative trends of these species in the two flames well (see Fig. 10a-c).

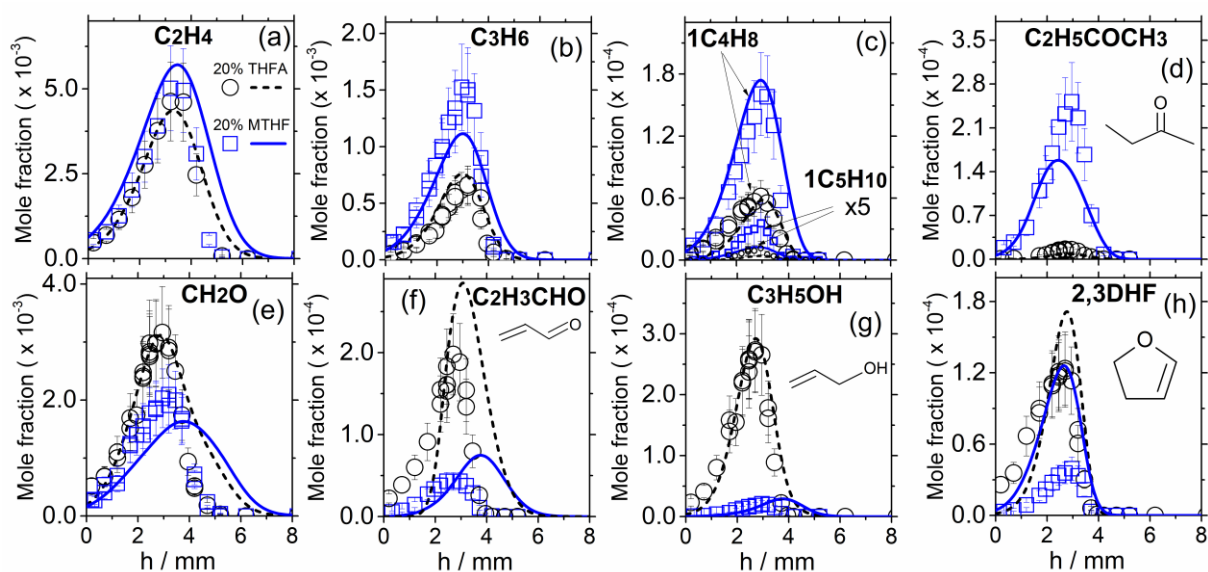


Fig. 10. THFA vs. MTHF: Mole fraction profiles of selected species that most influence the difference in mole fraction of the respective species family (highlighted in **bold** in Fig. 9b). For clarity, the indicated multiplication factor was used (for both experiment and model) for $1C_5H_{10}$. *Symbols*: experiment (initial conditions in Table 2), *lines*: present model. The experimental data of the 20% THFA flame is taken from [46]. The error bar for the experimental data is given.

Ketones: Their formation is highly favored in the 20% MTHF flame, which leads to a total amount of ketones that is about 10 times higher than that in the 20% THFA flame (Fig. 9b). All detected ketones were measured in larger amounts in the 20% MTHF flame. $C_2H_5COCH_3$ is the most abundant ketone in the MTHF flame and only produced in small quantities in the THFA flame. The kinetic model captures this difference well (Fig. 10d). This species has the largest impact on the difference of the total amount of ketone. As mentioned earlier, $cyC_3H_5COCH_3$ and $sC_3H_5COCH_3$ were only detected in the MTHF flame. Dubnikova

and Lifshitz [67] suggest (see Fig. 11) that these ketones can be produced from ring opening of MDHF, which is not formed from THFA but can be formed through C–H β -scission of the MTHF radicals.

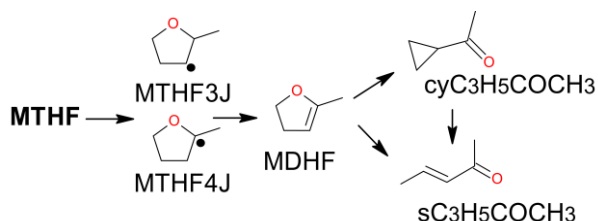


Fig. 11. Isomerization of MDHF, which is produced from MTHF, to form ketones (adapted from [67]).

Aldehydes: CH_3CHO and $\text{C}_2\text{H}_5\text{CHO}$ were measured in the two flames in similar quantities, but eight other aldehydes are produced in higher mole fractions in the 20% THFA flame than in the 20% MTHF flame (Fig. 9a). For example, $\text{C}_2\text{H}_3\text{CHO}$ is formed in about six times higher concentration in the 20% THFA flame than in the MTHF flame. Similarly, the THFA flame produces about 50% more CH_2O than the MTHF flame. Given their strong presence, CH_2O and $\text{C}_2\text{H}_3\text{CHO}$ controls the overall difference in aldehyde formation between the two flames. The present model reproduces this relative trend very well (Fig. 10e,f).

Alcohols: The experimentally observed total yield of alcohols is ~ 2.4 times higher in the THFA flame than in the MTHF flame (Fig. 9a). Four alcohols have been identified: CH_3OH , $\text{C}_2\text{H}_5\text{OH}$, $\text{C}_3\text{H}_5\text{OH}$, $4\text{C}_5\text{H}_9\text{OH}$ (Fig. 9b), but $4\text{C}_5\text{H}_9\text{OH}$ was solely detected in the MTHF flame and only in very small amounts (~ 4 ppm, Table S3). Its formation pathway, a pericyclic ring opening reaction proposed by De Bruycker *et al.* [30], is unique to MTHF. Among the other three alcohols, CH_3OH and $\text{C}_3\text{H}_5\text{OH}$ are formed in high concentrations, especially in the THFA flame. While the CH_3OH yields are not very different for the two flames, $\text{C}_3\text{H}_5\text{OH}$ (8 times higher in the THFA flame) is the decisive species making the difference in total alcohol yield between the two flames. The model predicts the trend of $\text{C}_3\text{H}_5\text{OH}$ very well (Fig. 10g).

Ethers: MDHF and 3,4DHP are special cases among the six ethers identified, because MDHF is only detected in the MTHF flame and 3,4DHP only in the THFA flame as mentioned

earlier. The 3,4DHP formation has already been discussed above and MDHF is simply a C–H β -scission product of the MTHF3J and MTHF4J radicals (Fig. 11). The remaining four identified ethers are CH₃OCH₃, C₃H₆O_{1,2}, furan, and 2,3DHF. CH₃OCH₃ and C₃H₆O_{1,2} are only slightly lower in the THFA flame than in the MTHF flame. 2,3DHF is formed in high concentrations and about three times more in the THFA flame than in the MTHF flame causing the total ether yield in the THFA flame to be about two times higher (Fig. 9b). As already discussed above, the model tends to overpredict 2,3DHF formation. The deviation is moderate in the THFA flame (about 20-30%) but severe (a factor of almost three) in the MTHF flame. Nevertheless, the trend that this species is produced in higher concentrations in the THFA flame is captured (Fig. 10h).

3.2.4. Comparison of important pathways in the 20% MTHF and 20% THFA flames

Before discussing the reaction pathways, we present the chemical structure, the bond-dissociation energies (BDEs) and the standard formation enthalpy for THFA and MTHF in Fig. 12. Both fuels have some similar features. The bond strengths of the weakest C–H bonds in both fuels are quite similar and the same holds for the C_{ring}–C_{lateral} bond, with considering the uncertainty of ± 1 kcal/mol of the calculation method. However, due to the partial oxidation of the CH₃ group to CH₂OH THFA has a lower standard enthalpy of formation than MTHF. Furthermore, as discussed in [46] the H-atom of OH is found to be in close proximity to the ether O-atom, creating a strong intramolecular hydrogen bond. This increases the BDE of the O–H bond (107.6 kcal/mol), which is higher than that of regular linear alcohols (e.g. ~105 kcal/mol for ethanol). The difference in the chemical structure of the two tetrahydrofuranic biofuels explains the differences in the formation of chemical species in the 20% THFA and 20% MTHF flames as presented above. A reaction pathway analysis below will exemplarily show how the fuel structure affects the formation of products.

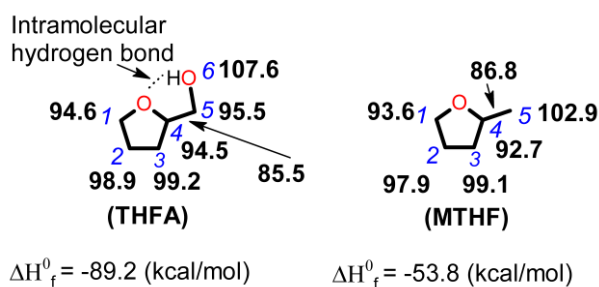


Fig. 12. THFA vs MTHF: chemical structure. *Italic* font: carbon/oxygen position, **bold** font: C–H, O–H, or C–C BDE in kcal/mol. BDEs of THFA were calculated in [46], while those of MTHF are calculated in the present work using the same methodology as in [46]. ΔH_f^0 is the standard enthalpy of formation.

Figure 13 presents comparatively the pathways between MTHF and THFA that lead to the formation of the most significant products pointed out in Section 3.2.3.

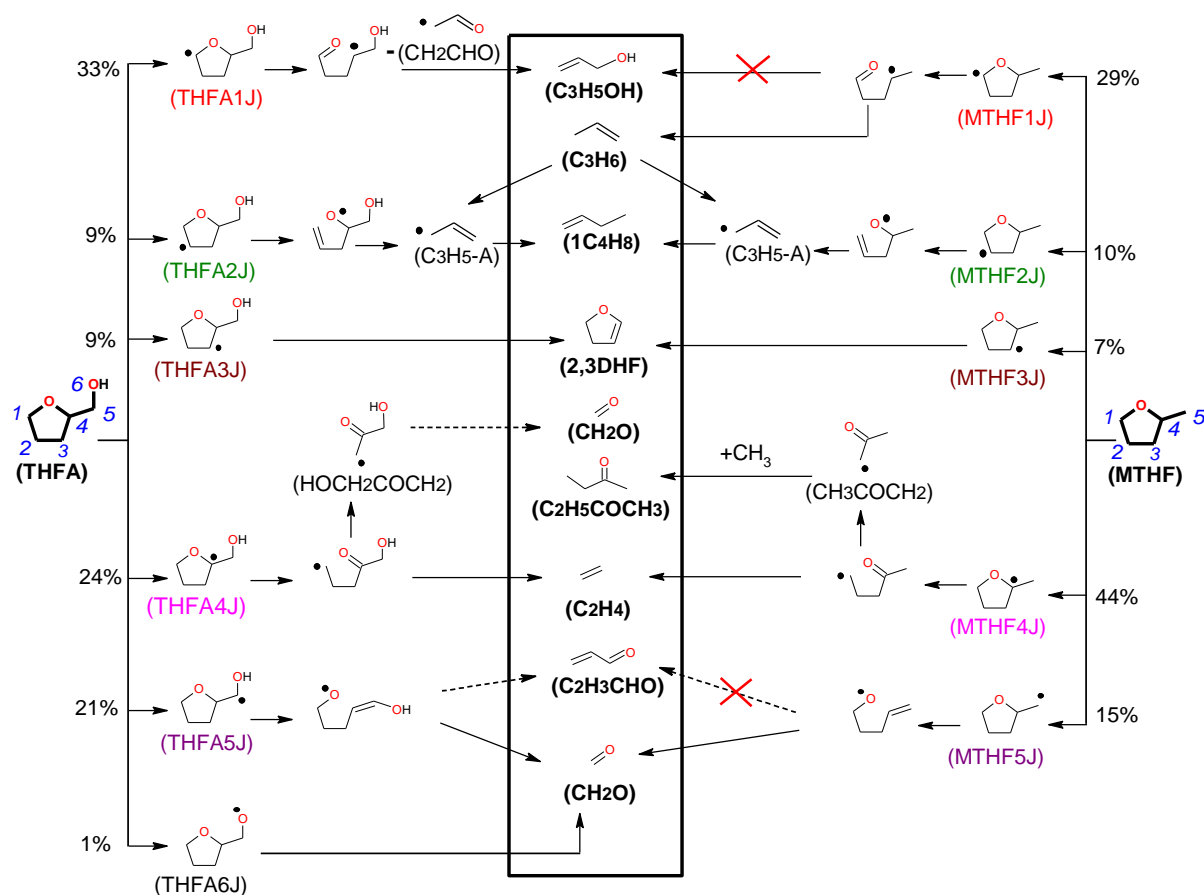


Fig. 13. Comparative analysis of THFA and MTHF reaction pathways (simplified) that lead to the formation of the important products discussed in Section 3.2.3, using the present model. The analysis was performed for the entire range (0-100%) of THFA or MTHF conversion. Percentages are the relative contributions of the respective pathway to fuel consumption. Dashed arrows indicate the inclusion of different steps (see Fig. S8 for details). Numbers in blue with *italic* font near the fuel structure label the carbon and oxygen positions.

At the flame conditions studied, the two biofuels are mainly consumed through H-abstractions. H-abstractions at C1 position of THFA and MTHF form the THFA1J and MTHF1J radicals, which lead directly to the formation of C_3H_5OH and C_3H_6 , respectively. This explains why C_3H_5OH was formed in larger amounts in the THFA flame, and C_3H_6 appears in higher concentrations in the MTHF flame. In both flames, $1C_4H_8$ is formed mainly via the recombination of C_3H_5-A and CH_3 . High C_3H_6 concentrations together with a slightly lower C2–H BDE (enhancing MTHF2J formation) favor the formation of $1C_4H_8$ in the MTHF flame, since both factors increase the concentration of the C_3H_5-A radicals.

2,3DHF is produced from the THFA3J or MTHF3J radicals. According to Fig. 13, about 9% of THFA is converted to the THFA3J radical which explains the high yields of 2,3DHF in this flame. The three times lower peak concentration of 2,3DHF in the MTHF flame suggests that the MTHF3J radical plays a less significant role in the MTHF decomposition, which is confirmed by the reaction analysis shown in Fig. 13.

H-abstraction reactions at the C4 position of MTHF followed by β -scission (C_2H_4 release) leads to the formation of 2-oxopropyl radical (CH_3COCH_2) which in turn reacts to form different ketones, *e.g.* by combining with CH_3 forming $C_2H_5COCH_3$, which was experimentally measured with the highest mole fraction among the detected ketones. The equivalent pathway in THFA also yields C_2H_4 but not the CH_3COCH_2 radical. This explains why ketones were quantified in much smaller amounts in the THFA flame. Instead 3-hydroxyketopropyl radical (CH_2COCH_2OH) is formed and this highly oxidized radical could produce ketene and CH_2OH , which in the presence of oxygen converts to CH_2O .

H-abstraction reactions at the C5 position of THFA and MTHF produce THFA5J and MTHF5J, respectively. While the ring opening of THFA5J leads to the formation of C_2H_3CHO , this aldehyde cannot be produced from the corresponding route of MTHF5J. Therefore, the C_2H_3CHO mole fraction is higher in the THFA flame than in the MTHF flame. Both fuels can

produce CH₂O via THFA5J or MTHF5J, respectively. However, THFA5J formation plays a larger role in the THFA flame (21%) compared to the 15% contribution of MTHF5J formation in the MTHF flame. This in part explains the higher CH₂O yield in the THFA flame.

Although CH₂O is produced in several secondary pathways (*e.g.* CH₃ + O), the alcohol group in THFA provides an extra formation route for CH₂O through β-scission of the THFA6J radical. It also enhances some other CH₂O formation pathways via THFA4J and THFA5J as discussed in the above paragraphs. Since analogous channels do not exist (or are less important) in MTHF, these pathways contribute to the higher CH₂O amount in the THFA flame compared to the MTHF flame.

As pointed out above, the intermediate species are mainly produced via H-abstractions and subsequent β-scissions of the resulting radicals. Therefore, the interpretation of the results does not require new chemistry but the thorough application of known pathways. One relatively subtle effect of the CH₂OH compared to the CH₃ group is to cause small bond energetic changes, which lead to slightly different contributions of the various pathways. A more important impact, however, is that the extra oxygen in THFA remains present in the primary products (mainly fuel radicals), which through subsequent reactions produce larger yields of higher oxidized products (*e.g.* aldehydes) compared to the corresponding MTHF chemistry. The main focus of the present study is in the formation and reactions of the primary species generated from biofuels. A full understanding of all product yields formed would require a thorough analysis and revision of the secondary chemistry. This could be an interesting subject of a future study.

Regarding the interactions between each of the studied biofuels and CH₄, while several possibilities are discussed in Section 2.3 and summarized in Fig. S6, only a few reactions have a notable impact (based on rate of reaction analyses). These are H-abstraction reactions from THFA and MTHF by CH₃. In the present THFA and MTHF flames, CH₄ contributes to ~40%

and 70% of the CH_3 yields at 1000 K and 1250 K, respectively. CH_3 also reacts with abundant radicals from biofuels, *e.g.* CH_2CHO , $\text{C}_3\text{H}_5\text{-A}$, CH_3COCH_2 (see their structure on Fig. 13). Because the same cross-reactions are important in both biofuel/methane flames and since the CH_4 concentration is similar in both flames, interaction chemistry is not expected to be responsible for differences seen in the 20% THFA/ CH_4 and 20% MTHF/ CH_4 flames.

4. Conclusions

This paper reports new speciation data for the low-pressure stoichiometric premixed methane flames which were either doped with 10% THFA or 20% MTHF at otherwise identical conditions. These flames were compared to a 20% THFA in methane flame reported in a previous study [46]. The two THFA flames together with data of the undoped methane flame allowed to explore the THFA specific chemistry as well as the influence of THFA concentration on the product yields. THFA and MTHF are both C_5 tetrahydrofuran derivatives and the 20% doped flames were used to identify common and fuel specific products including some highly toxic oxygenated species. Simulations with the slightly updated kinetic model proposed in [46] lead generally to good agreements with the experimental data. It captured well the fuel effects on the flame structure. The main results and conclusions are as follows:

- i) Compared to the neat methane flame (16 detected species) doping with THFA or MTHF drastically increases the number of detectable intermediate species (>40 species).
- ii) Doping with biofuel changes the final products only mildly, while it strongly modifies the concentrations of intermediate species.
- iii) The chemistry of the 10% THFA doped methane flame is similar to that of the 20% THFA doped flame with respect to product distributions and consumption pathways.

- iv) The peak mole fractions of most intermediate species approximately double when going from 10% to 20% doping with THFA. However, some species do not follow this trend and indicate interaction chemistry between methane and THFA.
- v) The differences in the chemical structure of THFA and MTHF do not influence significantly the mole fractions of the major products, which confirms that these products depend mostly on the initial C/O and C/H ratios of the inlet mixture.
- vi) THFA and MTHF show significant differences in the formation of intermediates species, including several toxic components (formaldehyde, acetaldehyde, allyl alcohol, etc.). Larger amounts of hydrocarbons and ketones were formed in the doped MTHF flame, whereas aldehydes, alcohols, and ethers are more abundant in the THFA doped flame. Reaction pathways analyses showed that the formation of these species is related to the chemical structure of biofuels.
- vii) The kinetic model generally reproduces the flame data well and proved to be very useful in the data interpretation. Nevertheless, some deviations are clearly larger than the experimental error, which suggest that further improvements are needed.

Future work is needed to comparatively investigate the two biofuels under fuel-rich flame conditions to evaluate their tendency to produce polycyclic aromatic hydrocarbon and soot. Furthermore, the formation of NO_x and other potential nitrogen-containing compounds for the studied fuel mixtures is a highly interesting topic for future studies. It would also be useful to evaluate the emission potential of the two biofuels in real engines, *e.g.* to test the likelihood for intermediate products such as aldehydes to be released in the exhaust gas stream.

Acknowledgments

This work is a contribution to the CPER research project CLIMIBIO. The authors thank the French Ministère de l'Enseignement Supérieur et de la Recherche, the Hauts-de-France Region

and the European Funds for Regional Economical Development for their financial support to this project. LST acknowledges the support from I-SITE via the Biofuel-Soot project (R-JEUNES CHERCHEURS-19-010-TRAN). Partial support from the IRePSE institute and the Laboratory of Excellence CaPPA is greatly appreciated. HHC acknowledges I3A for the use of its HPC cluster HERMES and the funding from the Aragón Government (Ref. T22_20R), co-funded by FEDER 2014-2020 "Construyendo Europa desde Aragón".

References

- [1] L. Lešnik, B. Kegl, E. Torres-Jiménez, F. Cruz-Peragón, Why we should invest further in the development of internal combustion engines for road applications, *Oil Gas Sci. Technol. – Rev. IFP Energies Nouvelles*. 75 (2020) 56. <https://doi.org/10.2516/ogst/2020051>.
- [2] BP Energy Outlook: 2020 Edition, available under www.bp.com, accessed October 16, 2020, 2020.
- [3] EASAC policy report 37, Decarbonisation of transport: Options and challenges., available under www.easac.eu, 2019. <https://easac.eu/publications/details/decarbonisation-of-transport-options-and-challenges/> (accessed October 16, 2020).
- [4] Transport & Environment, Globiom: the basis for biofuel policy post-2020, 2016. <https://www.transportenvironment.org/publications/globiom-basis-biofuel-policy-post-2020> (accessed January 29, 2018).
- [5] European Commission, Directorate-General for Energy, Proposal for a DIRECTIVE OF THE EUROPEAN PARLIAMENT AND OF THE COUNCIL on the promotion of the use of energy from renewable sources (recast), 2017. <http://eur-lex.europa.eu/legal-content/EN/TXT/?uri=CELEX:52016PC0767R%2801%29> (accessed May 30, 2018).
- [6] B. Flach, S. Lieberz, A. Rossetti, S. Phillips, EU-28: Biofuels Annual. EU Biofuels Annual 2017, United States Department of Agriculture, 2017. <https://www.fas.usda.gov/data/eu-28-biofuels-annual> (accessed February 2, 2018).
- [7] C. Ternel, A. Bouter, J. Melgar, Life cycle assessment of mid-range passenger cars powered by liquid and gaseous biofuels: Comparison with greenhouse gas emissions of electric vehicles and forecast to 2030, *Transportation Research Part D: Transport and Environment*. 97 (2021) 102897. <https://doi.org/10.1016/j.trd.2021.102897>.
- [8] M. Prussi, M. Yugo, L. Lonza, L. De Prada, M. Padella, R. Edwards, L. Lonza, JEC well-to-tank report V5, EUR 30269 EN, Publications Office of the European Union, Luxembourg. (2020) ISBN 978-92-76-19926-7. JRC119036. <https://doi.org/10.2760/959137>.
- [9] W. Leitner, J. Klankermayer, S. Pischinger, H. Pitsch, K. Kohse-Höinghaus, Advanced biofuels and beyond: Chemistry solutions for propulsion and production, *Angew. Chem.-Int. Edit.* 56 (2017) 5412–5452. <https://doi.org/10.1002/anie.201607257>.
- [10] T.W. Rudolph, J.J. Thomas, NO_x, NMHC and CO emissions from biomass derived gasoline extenders, *Biomass*. 16 (1988) 33–49. [https://doi.org/10.1016/0144-4565\(88\)90014-5](https://doi.org/10.1016/0144-4565(88)90014-5).
- [11] A. Sudholt, L. Cai, J. Heyne, F.M. Haas, H. Pitsch, F.L. Dryer, Ignition characteristics of a bio-derived class of saturated and unsaturated furans for engine applications, *Proc. Combust. Inst.* 35 (2015) 2957–2965. <https://doi.org/10.1016/j.proci.2014.06.147>.

- [12] S.F. Paul, Alternative fuel, No de brevet 5697987, United States Patent and Trademark Office, 1997.
- [13] S.F. Paul, An optimized alternative motor fuel formulation : natural gas liquids, ethanol, and a biomass-derived ether, Prepr. Symp. Am. Chem. Soc., Div. Fuel Chem. 43 (1998) 373–377.
- [14] DOE, P-series fuels. Part II, Federal Register. 64 (1999) 26822–26829.
- [15] M. Dahmen, W. Marquardt, Model-based design of tailor-made biofuels, *Energy Fuels*. 30 (2016) 1109–1134. <https://doi.org/10.1021/acs.energyfuels.5b02674>.
- [16] Y. Wu, X. Zhang, Z. Zhang, X. Wang, Z. Geng, C. Jin, H. Liu, M. Yao, Effects of diesel-ethanol-THF blend fuel on the performance and exhaust emissions on a heavy-duty diesel engine, *Fuel*. 271 (2020) 117633. <https://doi.org/10.1016/j.fuel.2020.117633>.
- [17] F. Mathieu, M. Reddemann, D. Martin, R. Kneer, Experimental investigation of fuel influence on atomization and spray propagation using an outwardly opening GDI-injector, *SAE Technical Papers*. (2010). <https://doi.org/10.4271/2010-01-2275>.
- [18] B. Aydoğan, Experimental investigation of tetrahydrofuran combustion in homogeneous charge compression ignition (HCCI) engine: Effects of excess air coefficient, engine speed and inlet air temperature, *Journal of the Energy Institute*. 93 (2020) 1163–1176. <https://doi.org/10.1016/j.joei.2019.10.009>.
- [19] J.-P. Lange, E. van der Heide, J. van Buijtenen, R. Price, Furfural - A promising platform for lignocellulosic biofuels, *ChemSusChem*. 5 (2012) 150–166. <https://doi.org/10.1002/cssc.201100648>.
- [20] Z. Yi, H. Xu, D. Hu, K. Yan, Facile synthesis of supported Pd catalysts by chemical fluid deposition method for selective hydrogenation of biomass-derived furfural, *J. Alloys Compd*. 799 (2019) 59–65. <https://doi.org/10.1016/j.jallcom.2019.05.350>.
- [21] A. Banerjee, S.H. Mushrif, Reaction pathways for the deoxygenation of biomass-pyrolysis-derived bio-oil on Ru: a DFT study using furfural as a model compound, *ChemCatChem*. 9 (2017) 2828–2838. <https://doi.org/10.1002/cctc.201700036>.
- [22] D. Hu, H. Xu, Z. Yi, Z. Chen, C. Ye, Z. Wu, H.F. Garces, K. Yan, Green CO₂-assisted synthesis of mono- and bimetallic Pd/Pt nanoparticles on porous carbon fabricated from sorghum for highly selective hydrogenation of furfural, *ACS Sustainable Chem. Eng.* 7 (2019) 15339–15345. <https://doi.org/10.1021/acssuschemeng.9b02665>.
- [23] W. Yang, A. Sen, One-step catalytic transformation of carbohydrates and cellulosic biomass to 2,5-dimethyltetrahydrofuran for liquid fuels, *ChemSusChem*. 3 (2010) 597–603. <https://doi.org/10.1002/cssc.200900285>.
- [24] J. Long, Q. Zhang, T. Wang, X. Zhang, Y. Xu, L. Ma, An efficient and economical process for lignin depolymerization in biomass-derived solvent tetrahydrofuran, *Bioresource Technology*. 154 (2014) 10–17. <https://doi.org/10.1016/j.biortech.2013.12.020>.
- [25] L.S. Tran, B. Sirjean, P.-A. Glaude, R. Fournet, F. Battin-Leclerc, Progress in detailed kinetic modeling of the combustion of oxygenated components of biofuels, *Energy*. 43 (2012) 4–18. <https://doi.org/10.1016/j.energy.2011.11.013>.
- [26] J.M. Simmie, Kinetics and thermochemistry of 2,5-dimethyltetrahydrofuran and related oxolanes : next-generation biofuels, *J. Phys. Chem. A*. 116 (2012) 4528–4538. <https://doi.org/10.1021/jp301870w>.
- [27] M.D. Boot, M. Tian, E.J.M. Hensen, S. Mani Sarathy, Impact of fuel molecular structure on auto-ignition behavior – Design rules for future high performance gasolines, *Prog. Energy Combust. Sci.* 60 (2017) 1–25. <https://doi.org/10.1016/j.pecs.2016.12.001>.
- [28] M. Tian, R.L. McCormick, J. Luecke, E. de Jong, J.C. van der Waal, G.P.M. van Klink, M.D. Boot, Anti-knock quality of sugar derived levulinic esters and cyclic ethers, *Fuel*. 202 (2017) 414–425. <https://doi.org/10.1016/j.fuel.2017.04.027>.

- [29] Y. Fenard, H. Song, H. Minwegen, P. Parab, C. Sampaio Mergulhão, G. Vanhove, K.-A. Heufer, 2,5-Dimethyltetrahydrofuran combustion: Ignition delay times at high and low temperatures, speciation measurements and detailed kinetic modeling, *Combust. Flame*. 203 (2019) 341–351. <https://doi.org/10.1016/j.combustflame.2019.02.022>.
- [30] R. De Bruycker, L.-S. Tran, H.-H. Carstensen, P.-A. Glaude, F. Monge, M.U. Alzueta, F. Battin-Leclerc, K.M. Van Geem, Experimental and modeling study of the pyrolysis and combustion of 2-methyl-tetrahydrofuran, *Combust. Flame*. 176 (2017) 409–428. <https://doi.org/10.1016/j.combustflame.2016.11.017>.
- [31] L. Cai, H. Minwegen, J. Beeckmann, U. Burke, R. Tripathi, A. Ramalingam, L.C. Kröger, A. Sudholt, K. Leonhard, J. Klankermayer, K.A. Heufer, H. Pitsch, Experimental and numerical study of a novel biofuel: 2-Butyltetrahydrofuran, *Combust. Flame*. 178 (2017) 257–267. <https://doi.org/10.1016/j.combustflame.2016.12.021>.
- [32] K. Moshhammer, S. Vranckx, H.K. Chakravarty, P. Parab, R.X. Fernandes, K. Kohse-Höinghaus, An experimental and kinetic modeling study of 2-methyltetrahydrofuran flames, *Combust. Flame*, 160 (2013) 2729–2743. <https://doi.org/10.1016/j.combustflame.2013.07.006>.
- [33] A. Sudholt, C. Lee, J. Klankermayer, R.X. Fernandes, H. Pitsch, Ignition characteristics of saturated and unsaturated furans, *Combust. Flame*. 171 (2016) 133–136. <https://doi.org/10.1016/j.combustflame.2016.05.016>.
- [34] L.-S. Tran, M. Verdicchio, F. Monge, R.C. Martin, R. Bounaceur, B. Sirjean, P.-A. Glaude, M.U. Alzueta, F. Battin-Leclerc, An experimental and modeling study of the combustion of tetrahydrofuran, *Combust. Flame*. 162 (2015) 1899–1918. <https://doi.org/10.1016/j.combustflame.2014.12.010>.
- [35] P. Dagaut, M. McGuinness, J.M. Simmie, M. Cathonnet, The ignition and oxidation of tetrahydrofuran: experiments and kinetic modeling, *Combust. Sci. Technol.* 135 (1998) 3–29. <https://doi.org/10.1080/00102209808924147>.
- [36] X. Wang, R. Chen, B. He, D. Li, M. Qin, X. Fan, Laminar flame characteristics of THF family fuels at elevated temperatures and pressures, *Fuel*. 273 (2020) 117721. <https://doi.org/10.1016/j.fuel.2020.117721>.
- [37] Y. Wu, N. Xu, M. Yang, Y. Liu, C. Tang, Z. Huang, Ignition delay time measurement and kinetic modeling of furan, and comparative studies of 2,3-dihydrofuran and tetrahydrofuran at low to intermediate temperatures by using a rapid compression machine, *Combust. Flame*. 213 (2020) 226–236. <https://doi.org/10.1016/j.combustflame.2019.12.010>.
- [38] Y. Li, W. Xu, Y. Jiang, K.M. Liew, R. Qiu, Laminar burning velocities of 2-methyltetrahydrofuran at elevated pressures, *Proc. Combust. Inst.* 38 (2021) 2175–2183. <https://doi.org/10.1016/j.proci.2020.06.253>.
- [39] R.B.R. da Costa, R.M. Valle, J.J. Hernández, A.C.T. Malaquias, C.J.R. Coronado, F.J.P. Pujatti, Experimental investigation on the potential of biogas/ethanol dual-fuel spark-ignition engine for power generation: Combustion, performance and pollutant emission analysis, *Applied Energy*. 261 (2020) 114438. <https://doi.org/10.1016/j.apenergy.2019.114438>.
- [40] X. Zheng, S. Jouzdani, B. Akih-Kumgeh, Auto ignition study of methane and bio alcohol fuel blends, *J. Eng. Gas Turbines Power*. 141 (2019). <https://doi.org/10.1115/1.4045345>.
- [41] Y. Li, J. Xue, J. Peppers, N.Y. Kado, C.F.A. Vogel, C.P. Alaimo, P.G. Green, R. Zhang, B.M. Jenkins, M. Kim, T.M. Young, M.J. Kleeman, Chemical and Toxicological Properties of Emissions from a Light-Duty Compressed Natural Gas Vehicle Fueled with Renewable Natural Gas, *Environ. Sci. Technol.* 55 (2021) 2820–2830. <https://doi.org/10.1021/acs.est.0c04962>.

- [42] J. Wang, X. Wang, X. Fan, K. Yang, Shock tube experimental and modeling study of MTHF ignition characteristics at high temperatures, SAE International, Warrendale, PA, 2015. <https://doi.org/10.4271/2015-01-1807>.
- [43] R. Tripathi, C. Lee, R.X. Fernandes, H. Olivier, H.J. Curran, S. Mani Sarathy, H. Pitsch, Ignition characteristics of 2-methyltetrahydrofuran: An experimental and kinetic study, *Proc. Combust. Inst.* 36 (2017) 587–595. <https://doi.org/10.1016/j.proci.2016.07.103>.
- [44] S. Jouzdani, X. Zheng, A. Zhou, B. Akih-Kumgeh, Shock tube investigation of methyl tert butyl ether and methyl tetrahydrofuran high-temperature kinetics, *Int. J. Chem. Kinet.* 51 (2019) 848–860. <https://doi.org/10.1002/kin.21314>.
- [45] Y. Fenard, M.A. Boumehdi, G. Vanhove, Experimental and kinetic modeling study of 2-methyltetrahydrofuran oxidation under engine-relevant conditions, *Combust Flame.* 178 (2017) 168–181. <https://doi.org/10.1016/j.combustflame.2017.01.008>.
- [46] L.-S. Tran, H.-H. Carstensen, K.K. Foo, N. Lamoureux, S. Gosselin, L. Gasnot, A. El-Bakali, P. Desgroux, Experimental and modeling study of the high-temperature combustion chemistry of tetrahydrofurfuryl alcohol, *Proc. Combust. Inst.* 38 (2021) 631–640. <https://doi.org/10.1016/j.proci.2020.07.057>.
- [47] M. Braun-Unkhoff, N. Hansen, M. Dietrich, T. Methling, K. Moshhammer, B. Yang, Entanglement of n-heptane and iso-butanol chemistries in flames fueled by their mixtures, *Proc. Combust. Inst.* 38 (2021) 2387–2395. <https://doi.org/10.1016/j.proci.2020.06.103>.
- [48] L.-S. Tran, Y. Li, M. Zeng, J. Pieper, F. Qi, F. Battin-Leclerc, K. Kohse-Höinghaus, O. Herbinet, Elevated pressure low-temperature oxidation of linear five-heavy-atom fuels: diethyl ether, n-pentane, and their mixture, *Z. Physik. Chem.* 234 (2020) 1269–1293. <https://doi.org/10.1515/zpch-2020-1613>.
- [49] L.-S. Tran, J. Pieper, M. Zeng, Y. Li, X. Zhang, W. Li, I. Graf, F. Qi, K. Kohse-Höinghaus, Influence of the biofuel isomers diethyl ether and n-butanol on flame structure and pollutant formation in premixed n-butane flames, *Combust. Flame.* 175 (2017) 47–59. <https://doi.org/10.1016/j.combustflame.2016.06.031>.
- [50] A.M. Dmitriev, D.A. Knyazkov, T.A. Bolshova, A.G. Shmakov, O.P. Korobeinichev, The effect of methyl pentanoate addition on the structure of premixed fuel-rich n-heptane/toluene flame at atmospheric pressure, *Combust. Flame.* 162 (2015) 1964–1975. <https://doi.org/10.1016/j.combustflame.2014.12.015>.
- [51] K.K. Foo, N. Lamoureux, A. Cessou, C. Lacour, P. Desgroux, The accuracy and precision of multi-line NO-LIF thermometry in a wide range of pressures and temperatures, *J. Quant. Spectrosc. Radiat. Transfer.* 255 (2020) 107257. <https://doi.org/10.1016/j.jqsrt.2020.107257>.
- [52] N. Lamoureux, P. Desgroux, A. El Bakali, J.F. Pauwels, Experimental and numerical study of the role of NCN in prompt-NO formation in low-pressure CH₄-O₂-N₂ and C₂H₂-O₂-N₂ flames, *Combust. Flame.* 157 (2010) 1929–1941. <https://doi.org/10.1016/j.combustflame.2010.03.013>.
- [53] Thermo NO-LIF program is downloadable at the website: <https://pc2a.univ-lille.fr/thermo-no-lif/>, (2021).
- [54] Chemkin-Pro 2019R1, ANSYS: Canonsburg, PA, 2019.
- [55] N. Lamoureux, P. Desgroux, In situ laser-induced fluorescence and ex situ cavity ring-down spectroscopy applied to no measurement in flames: microprobe perturbation and absolute quantification, *Energy Fuels.* 35 (2021) 7107–7120. <https://doi.org/10.1021/acs.energyfuels.0c03806>.
- [56] U. Struckmeier, P. Oßwald, T. Kasper, L. Boehling, M. Heusing, M. Koehler, A. Brockhinke, K. Kohse-Höinghaus, Sampling probe influences on temperature and species concentrations in molecular beam mass spectroscopic investigations of flat premixed low-

- pressure flames, *Z. Physik. Chem.* 223 (2009) 503–537. <https://doi.org/10.1524/zpch.2009.6049>.
- [57] S.M. Burke, W. Metcalfe, O. Herbinet, F. Battin-Leclerc, F.M. Haas, J. Santner, F.L. Dryer, H.J. Curran, An experimental and modeling study of propene oxidation. Part 1: Speciation measurements in jet-stirred and flow reactors, *Combust. Flame*. 161 (2014) 2765–2784. <https://doi.org/10.1016/j.combustflame.2014.05.010>.
- [58] S.M. Burke, U. Burke, R. Mc Donagh, O. Mathieu, I. Osorio, C. Keese, A. Morones, E.L. Petersen, W. Wang, T.A. DeVerter, M.A. Oehlschlaeger, B. Rhodes, R.K. Hanson, D.F. Davidson, B.W. Weber, C.-J. Sung, J. Santner, Y. Ju, F.M. Haas, F.L. Dryer, E.N. Volkov, E.J.K. Nilsson, A.A. Konnov, M. Alrefae, F. Khaled, A. Farooq, P. Dirrenberger, P.-A. Glaude, F. Battin-Leclerc, H.J. Curran, An experimental and modeling study of propene oxidation. Part 2: Ignition delay time and flame speed measurements, *Combust. Flame*. 162 (2015) 296–314. <https://doi.org/10.1016/j.combustflame.2014.07.032>.
- [59] M. Pelucchi, K.P. Somers, K. Yasunaga, U. Burke, A. Frassoldati, E. Ranzi, H.J. Curran, T. Faravelli, An experimental and kinetic modeling study of the pyrolysis and oxidation of n-C₃C₅ aldehydes in shock tubes, *Combust. Flame*. 162 (2015) 265–286. <https://doi.org/10.1016/j.combustflame.2014.07.027>.
- [60] F.H. Vermeire, R. De Bruycker, O. Herbinet, H.-H. Carstensen, F. Battin-Leclerc, G.B. Marin, K.M. Van Geem, Experimental and kinetic modeling study of the pyrolysis and oxidation of 1,5-hexadiene: The reactivity of allylic radicals and their role in the formation of aromatics, *Fuel*. 208 (2017) 779–790. <https://doi.org/10.1016/j.fuel.2017.07.042>.
- [61] C.W. Gao, J.W. Allen, W.H. Green, R.H. West, Reaction mechanism generator: Automatic construction of chemical kinetic mechanisms, *Comput. Phys. Commun.* 203 (2016) 212–225. <https://doi.org/10.1016/j.cpc.2016.02.013>.
- [62] L.-S. Tran, R. De Bruycker, H.-H. Carstensen, P.-A. Glaude, F. Monge, M.U. Alzueta, R.C. Martin, F. Battin-Leclerc, K.M. Van Geem, G.B. Marin, Pyrolysis and combustion chemistry of tetrahydropyran: Experimental and modeling study, *Combust. Flame*. 162 (2015) 4283–4303. <https://doi.org/10.1016/j.combustflame.2015.07.030>.
- [63] D. Liu, Kinetic analysis of the chemical effects of hydrogen addition on dimethyl ether flames, *Int. J. Hydrog. Energy*. 39 (2014) 13014–13019. <https://doi.org/10.1016/j.ijhydene.2014.06.072>.
- [64] D. Liu, J. Santner, C. Togbe, D. Felsmann, J. Koppmann, A. Lackner, X. Yang, X. Shen, Y. Ju, K. Kohse-Hoeinghaus, Flame structure and kinetic studies of carbon dioxide-diluted dimethyl ether flames at reduced and elevated pressures, *Combust. Flame*. 160 (2013) 2654–2668. <https://doi.org/10.1016/j.combustflame.2013.06.032>.
- [65] P.S. Veloo, Y.L. Wang, F.N. Egolfopoulos, C.K. Westbrook, A comparative experimental and computational study of methanol, ethanol, and n-butanol flames, *Combust. Flame*. 157 (2010) 1989–2004. <https://doi.org/10.1016/j.combustflame.2010.04.001>.
- [66] R. Daniel, L. Wei, H. Xu, C. Wang, M.L. Wyszynski, S. Shuai, Speciation of hydrocarbon and carbonyl emissions of 2,5-dimethylfuran combustion in a DISI engine, *Energy Fuels*. 26 (2012) 6661–6668. <https://doi.org/10.1021/ef301236f>.
- [67] F. Dubnikova, A. Lifshitz, Isomerization of 2,3-dihydrofuran and 5-methyl-2,3-dihydrofuran : quantum chemical and kinetics calculations, *J. Phys. Chem. A*. 106 (2002) 1026–1034. <https://doi.org/10.1021/jp012714h>.

List of Table Titles

Table 1 Relevant physicochemical properties of THFA and MTHF. Those of ethanol and conventional fuels are presented for comparison [9,17,25]. ^a at 298 K. ^bLHV: Lower Heating Value. RON: Research Octane Number.

Table 2 Flame conditions. Φ : equivalence ratio. P : pressure. R_{bio} : fraction of doped biofuel in the fuel mixture ($=\text{biofuel}/(\text{biofuel}+\text{CH}_4)$). Nl/min : normal liter per minute (101.3 kPa, 273.15 K). N_2 (~70%) was used as diluent.

Table 3 Rate coefficients of the newly added reactions for 4-pentenal ($4C_4H_7CHO$), *i.e.* those in Fig. 1. The rate coefficients ($k=AT^n\exp(-E_a/RT)$) are given in cm^3 , mol, s, cal units.

Table 4 Intermediates measured in the 10% THFA flame. SG : species group based on the number of heavy atoms (C and O). M : nominal mass (g/mol). x_{max} : peak mole fraction. *CPaldehyde*: Cyclopropanecarboxaldehyde. *THFaldehyde*: Tetrahydrofuran-2-aldehyde. **Bold**: highlighting the most abundant species in its respective SG. ***Bold Italic***: highlighting the next two abundant species (within a factor 3 compared to the highest one, except for furan)

Table 5 Conditions of the doped F-THFA flames. ^a Based on CH_4 and O_2 .

List of Figure Captions

Fig. 1 New reactions added for 4-pentenal ($4C_4H_7CHO$): (i) Retroene reaction and H migration, (ii) H-additions, (iii) OH-additions. The rate coefficients of these reactions are summarized in Table 3.

Fig. 2 Comparison of the mole fraction profiles of major species obtained in the 10% and 20% THFA flames: reactants (THFA, CH_4 , O_2) (a-c), diluent (N_2) (d), temperature (T) (e) and main products (CO_2 , CO, H_2 , H_2O) (f-l). *Symbols*: experimental data (see initial conditions in Table 2), *lines*: present model. The experimental data of the 20% THFA flame is taken from [46]. Error bars in this and following figures are based on the uncertainties discussed in Section 2.2

Fig. 3 Mole fraction profiles as a function of the height above the burner (h) of the most important intermediate species measured in the 10% THFA flame. *Symbols*: experimental data with estimated error bars (see initial conditions in Table 2), *lines*: present model

Fig. 4 Comparison of (normalized) experimental peak mole fraction of the three studied flames. Normalization was performed using the data of the 20% THFA flame as reference. For clarity, peaks of individual species of the 20% THFA flame are not shown but indicated as the horizontal red solid line. The experimental data of the 20% THFA flame is taken from [46]. Initial conditions are available in Table 2

Fig. 5 Comparison of mole fraction profiles of selected *fuel-specific decomposition* products of the 10% and 20% THFA flames. Species presented are those highlighted in **bold** font in Table 4, *i.e.*, the most abundant species of each species group. (a), (b), (c), (d), (e): two, three, four, five, six-seven heavy atom group, respectively. *Symbols*: experiment (see initial conditions in Table 2), *lines*: present model. The experimental data of the 20% THFA flame is taken from [46]

Fig. 6 Contribution of the individual fuel to the formation of combustion products. (a) Explanation how the contribution is calculated. *Symbols*: experiment. *Lines*: present model. (b,c) Selected simulation results. Initial conditions are available in Table 2 and Table 5

Fig. 7 20% THFA vs 20% MTHF flames: Mole fractions of the reactants and the major final products. *Symbols*: experiments (see initial conditions in Table 2), *lines*: present model. For clarity, the experimental and simulated profiles of biofuels (THFA and MTHF) were multiplied by a factor of 2. The experimental data of the 20% THFA flame is taken from [46]

Fig. 8 Mole fraction profiles of selected intermediate species detected in the MTHF flame. *Symbols*: experiment (see initial conditions in Table 2), *lines*: three available MTHF models (*Solid line*: present model. *Dashed lines*: model of Moshhammer *et al.* [32]. *Dotted lines*: model of Fenard *et al.*[45]). CH_3OCH_3 , furan, 2,3DHF, and $C_2H_5COCH_3$ are not present in the model of [32]

Fig. 9 Comparison of (normalized) experimental peak mole fraction between the 20% THFA and 20% MTHF flames (initial conditions in Table 2). **(a)** All intermediate species. **(b)** Sum of species in their respective family. Species highlighted in **bold** are those having the largest impact on the difference of the total amount of the respective species family. The experimental data of the 20% THFA flame is taken from [46].

Fig. 10 THFA vs. MTHF: Mole fraction profiles of selected species that most influence the difference in mole fraction of the respective species family (highlighted in **bold** in Fig. 9b). For clarity, the indicated multiplication factor was used (for both experiment and model) for $1C_5H_{10}$. *Symbols*: experiment (initial conditions in Table 2), *lines*: present model. The experimental data of the 20% THFA flame is taken from [46]. The error bar for the experimental data is given

Fig. 11 Isomerization of MDHF, which is produced from MTHF, to form ketones (adapted from [67]).

Fig. 12 THFA vs MTHF: chemical structure. *Italic* font: carbon/oxygen position, **bold** font: C–H, O–H, or C–C BDE in kcal/mol. BDEs of THFA were calculated in [46], while those of MTHF are calculated in the present work using the same methodology as in [46]. ΔH_f^0 is the standard enthalpy of formation

Fig. 13 Comparative analysis of THFA and MTHF reaction pathways (simplified) that lead to the formation of the important products discussed in Section 3.2.3, using the present model. The analysis was performed for the entire range (0-100%) of THFA or MTHF conversion. Percentages are the relative contributions of the respective pathway to fuel consumption. Dashed arrows indicate the inclusion of different steps (see Fig. S8 for details). Numbers in blue with *italic* font near the fuel structure label the carbon and oxygen positions.

List of Supplemental Information

- 1) Supplemental information (PDF)
- 2) Kinetic model (Text)
- 3) Experimental data (Excel)